



NRL/MR/6180--14-9563

Demonstration of Experimental Infrastructure for Studying Cell-to-Cell Failure Propagation in Lithium-ion Batteries

CHRISTOPHER R. FIELD
MARK H. HAMMOND
STEVEN G. TUTTLE
BRADLEY A. WILLIAMS
SUSAN L. ROSE-PEHRSSON

*Navy Technology Center for Safety and Survivability
Chemistry Division*

NEIL S. SPINNER
*National Academies of Science
Washington, DC*

KRISTINA M. MYERS
ADAM L. LUBRANO
*Nova Research, Inc.
Alexandria, Virginia*

September 11, 2014

Approved for public release; distribution is unlimited.

REPORT DOCUMENTATION PAGE				Form Approved OMB No. 0704-0188	
Public reporting burden for this collection of information is estimated to average 1 hour per response, including the time for reviewing instructions, searching existing data sources, gathering and maintaining the data needed, and completing and reviewing this collection of information. Send comments regarding this burden estimate or any other aspect of this collection of information, including suggestions for reducing this burden to Department of Defense, Washington Headquarters Services, Directorate for Information Operations and Reports (0704-0188), 1215 Jefferson Davis Highway, Suite 1204, Arlington, VA 22202-4302. Respondents should be aware that notwithstanding any other provision of law, no person shall be subject to any penalty for failing to comply with a collection of information if it does not display a currently valid OMB control number. PLEASE DO NOT RETURN YOUR FORM TO THE ABOVE ADDRESS.					
1. REPORT DATE (DD-MM-YYYY) 11-09-2014		2. REPORT TYPE Memorandum Report		3. DATES COVERED (From - To) March 2012 – December 2012	
4. TITLE AND SUBTITLE Demonstration of Experimental Infrastructure for Studying Cell-to-Cell Failure Propagation in Lithium-ion Batteries				5a. CONTRACT NUMBER	
				5b. GRANT NUMBER	
				5c. PROGRAM ELEMENT NUMBER 0602123N	
6. AUTHOR(S) Christopher R. Field, Mark H. Hammond, Steven G. Tuttle, Bradley A. Williams, Susan L. Rose-Pehrsson, Neil S. Spinner, ¹ Kristina M. Myers, ² and Adam L. Lubrano ²				5d. PROJECT NUMBER	
				5e. TASK NUMBER	
				5f. WORK UNIT NUMBER 61-9496-A-2-5	
7. PERFORMING ORGANIZATION NAME(S) AND ADDRESS(ES) Naval Research Laboratory 4555 Overlook Avenue, SW Washington, DC 20375-5320				8. PERFORMING ORGANIZATION REPORT NUMBER NRL/MR/6180--14-9563	
9. SPONSORING / MONITORING AGENCY NAME(S) AND ADDRESS(ES) Office of Naval Research One Liberty Center 875 North Randolph Street, Suite 1425 Arlington, VA 22203-1995				10. SPONSOR / MONITOR'S ACRONYM(S) ONR	
				11. SPONSOR / MONITOR'S REPORT NUMBER(S)	
12. DISTRIBUTION / AVAILABILITY STATEMENT Approved for public release; distribution is unlimited.					
13. SUPPLEMENTARY NOTES ¹ National Academies of Science, National Research Council, 500 Fifth Street, NW, Washington, DC 20001 ² Nova Research, Inc., 1900 Elkin Street, Suite 230, Alexandria, VA 22308					
14. ABSTRACT A 5 cubic meter decompression chamber was repurposed as a test chamber to conduct failure abuse experiments on commercial 18650-type lithium-ion batteries. Various modifications were performed to enable remote control and monitoring of chamber functions, along with collection of data from instrumentation during tests including high speed and infrared cameras, a Fourier transform infrared spectrometer, real-time gas analyzers, and compact reconfigurable input and output devices. Single- and multi-cell packages of LiCoO ₂ and LiFePO ₄ chemistry 18650 lithium-ion batteries were constructed and data was obtained and analyzed for abuse and failure tests. Observations from recorded camera videos, thermocouples, heat flux gauges, and gas analyses revealed qualitative insights into failure mechanisms and heat propagation from cell to cell. Future directions based on these observations are also proposed.					
15. SUBJECT TERMS Lithium-ion batteries 18650 cells Failure LiCoO ₂ Heat propagation LiFePO ₄					
16. SECURITY CLASSIFICATION OF:			17. LIMITATION OF ABSTRACT Unclassified Unlimited	18. NUMBER OF PAGES 37	19a. NAME OF RESPONSIBLE PERSON Susan L. Rose-Pehrsson
a. REPORT Unclassified Unlimited	b. ABSTRACT Unclassified Unlimited	c. THIS PAGE Unclassified Unlimited			19b. TELEPHONE NUMBER (include area code) (202) 767-3138

Contents

1.0 Background	1
2.0 Objective	2
3.0 Approach.....	2
3.1 Chamber Control System	3
3.2 Chamber Cameras	9
3.3 Real-Time Gas Analyzers and In-Situ FTIR	14
3.4 Surrogate Cells.....	16
3.5 Multiple Cell Packaging.....	17
4.0 Results.....	21
4.1 Single Cell Failure Event	21
4.2 Hex Package Cell-to-Cell Failure Events	23
5.0 Conclusions	32
6.0 References	33

1.0 Background

A key capability gap in assuring safe use of lithium-ion batteries is adequately protecting against the full range of impacts and consequences on neighboring cells in a large battery pack as one cell undergoes failure. While models do exist for commercial and Department of Energy (DOE) applications, such as automotive batteries [1-4], their use of experimental data to capture the impact on nearby cells of high temperatures, gas venting, fire, and shrapnel due to cell failure as related to Navy and shipboard applications has been limited. A predictive capability is needed to accurately determine a maximum credible event (MCE) for battery behavior and to extrapolate cell behavior to full scale battery systems used on Navy platforms, which will ultimately reduce cost in testing and certification.

Higher-level models that predict different aspects of platform impact, e.g. fire spread [5,6] and structural damage [7], will need modifications (i.e. additional modules) to describe and predict the consequences of catastrophic battery failure effects. These required modifications should be possible with upgrades that enable a more accurate description of battery casualty and can be directly fed into models. Conversely, lower-level thermo-electrochemical models and studies exist for describing the internal condition inside a single cell [8-11]. These models describing the internal chemistry and micro-structure of individual cells have provided valuable insights into the sources of cell failure, but fail to extend to multiple cells. Thus, there is a knowledge gap between single cell and large format (greater than 100 cells) lithium-ion battery failure.

Detailed testing to measure the impact of a single cell failure on nearby cells has been limited [12-16]. Because there are several different ways in which the failure of a single cell may spread to neighboring cells, a number of parameters must be measured to adequately document what conditions cause failure to spread. Thus, the Naval Research Laboratory (NRL) has been developing the necessary scientific and experimental infrastructure to investigate cell-to-cell failure propagation in lithium-ion batteries and provide robust experimental data for computational models.

NRL has a 5-m³ (177 ft³) two-man decompression chamber that has been re-purposed as an environmental test chamber located at the Chesapeake Bay Detachment (CBD) in Chesapeake Beach, Maryland, USA. Figure 1 shows an image of the chamber after its conversion to a test chamber.

The 5-m³ chamber has been used in a number of projects and experiments within the Navy Technology Center for Safety and Survivability, Code 6180, but most recently it has been used to investigate lithium-ion battery safety, specifically identifying the chemical species released during a single cell failure [17]. Numerous upgrades and revisions have been instituted to conduct these experiments, but none of the changes have had a coherent goal nor focused on implementing instrumentation and equipment for analysis of cell-to-cell failure propagation in larger format lithium-ion batteries. Herein, the focus is on developing and demonstrating the experimental infrastructure for investigating cell-to-cell failure propagation in lithium-ion batteries.

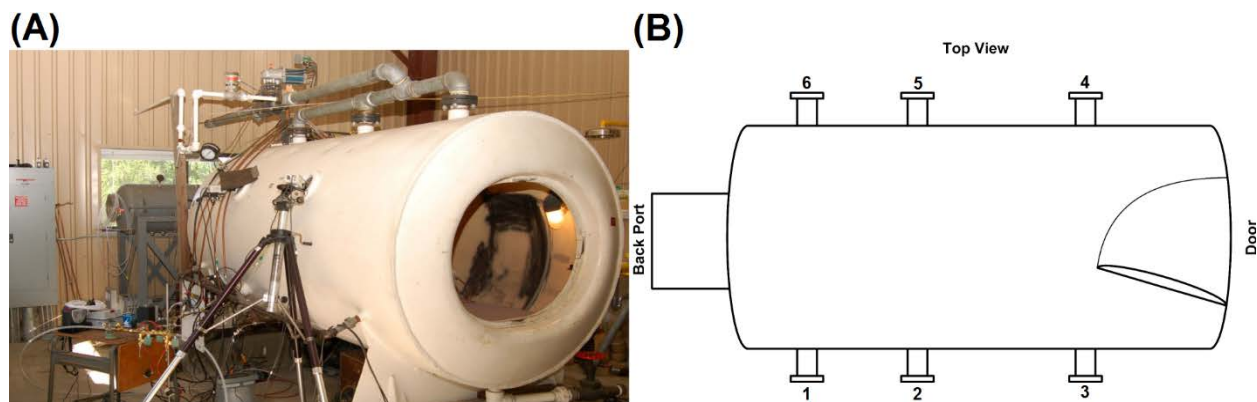


Figure 1: (A) An image of the two-man decompression chamber that has been re-purposed into a 5-m³ (177 ft³) environmental test chamber at the Chesapeake Bay Detachment (CBD) of the Naval Research Laboratory in Chesapeake Beach, Maryland, USA. (B) A diagram showing the top view of the chamber with two doors (Front and Back) and six ports (three on each side).

2.0 Objective

To demonstrate the facilities and capabilities for conducting investigations in cell-to-cell failure propagation and collect preliminary experimental data to guide the creation of a lithium-ion battery failure model.

3.0 Approach

The 5-m³ chamber at NRL-CBD was upgraded with a variety of new instrumentation and equipment to study cell-to-cell failure propagation in lithium-ion batteries. These upgrades included new bulkheads and pass-through configurations for the six ports along the perimeter of the chamber (three on each side), as seen in Figure 1. Ports 1 and 2 were used to pass the beam from the Fourier Transform Infrared (FTIR) spectrometer into and out of the chamber for *in situ*, real-time chemical species identification. Both ports received new mirrors which are 99.9% reflective in the IR region to improve the analytical capabilities of the *in situ* FTIR instrumentation. Port 3 was used for plumbing gas and liquid into and out of the chamber. Several of the seals and bulkheads for pipe connections were replaced to minimize leaks during experiments. Port 4 was mounted with two RJ45 Cat6, water tight Ethernet bulkhead connectors and two Bayonet Neill-Concelman (BNC) connectors for communication and electrical connections inside the chamber, respectively. Port 5 was given an 80 channel, water tight K-Type thermocouple bulkhead to make measurements of chamber temperatures during experiments. The previous plate on Port 6 had a series of small thermocouple bulkheads that was replaced with a blank plate since the 80 channel thermocouple plate was installed on Port 5. The blank plate on Port 6 could be replaced with another custom plate for experiments requiring additional functionality. Figure 2 shows a diagram summarizing the various port and plate configurations for the chamber.

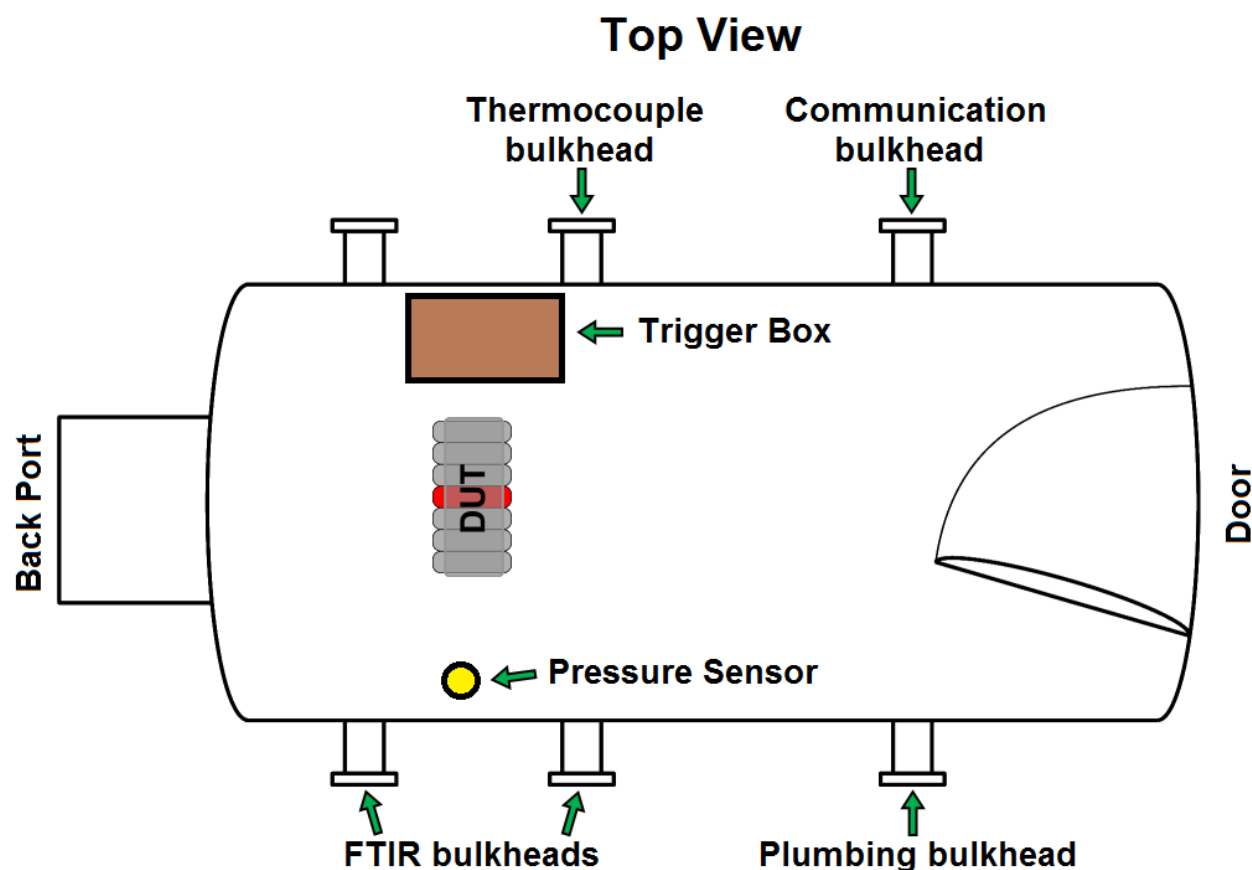


Figure 2: A diagram of the chamber showing locations of the thermocouple bulkhead, communication bulkhead, FTIR bulkheads, plumbing bulkhead, pressure sensor, trigger box, and approximate position of the device under test (DUT).

3.1 Chamber Control System

Control and monitoring of the chamber functions and conditions were upgraded to include a new system that enables a local or remote mode. The local mode consists of a control box mounted in the same building (CBD Building 310) and room as the chamber. The control box contains a series of manual switches that control the state of various components of the chamber. Each control includes a light indicator, a fuse, and a label of its function and maximum electrical amperage. Each switch controls an independent channel and electrical circuit so that a short on one channel does not shutdown all of the channels. Figure 3 shows an image of the control box and the various switches used to control the chamber components.

The control box is hard-wired (i.e. it cannot be disconnected) to the following chamber functions: Lights, Vent Valve, Exhaust Fan, Power, Vacuum Pump, Compressed Air Valve, Mixing Fan, and Compressed Gas Valve. In addition to these chamber functions, the control box is connected to two trigger boxes and three external channels that are user-configurable and have standard US, NEMA 5-15R three-prong female AC power outlets for powering various experimental instrumentation and equipment. One trigger box is located inside the chamber and has sixteen independent channels. The second trigger box is located underneath, but

outside, the chamber and is commonly referred to as the "Quad Box" because it has four independently activated/deactivated power channels. The three-channel external power circuit is located directly underneath the control box. Figure 4 shows images of the two trigger boxes and the external, three-channel power circuit.

The chamber is controlled locally by selecting the "Local" mode on the mode selector switch indicated in Figure 3. In Local mode, lights, vent valve, exhaust fan, trigger box channels, etc. can be activated and deactivated directly from the control box. Additionally, the control box features a male 32-pin D-sub miniature (DB32) connector that provides an interface for connecting an external control system to activate and deactivate chamber functions, but only if the mode selector switch is set to "Remote", as seen in Figure 3. Each pin in the DB32 connector is associated with a chamber function or channel on the control box. A chamber function or channel is activated by applying 5V referenced to ground to the pin and deactivated by applying 0V or shorting to ground. The pin assignments and corresponding chamber functions or activated channels are shown in Table 1.

A four-slot Compact Reconfigurable Input and Output (CompactRIO) was purchased from National Instruments (cRIO-9025, National Instruments, Inc., Austin, Texas, USA) to implement a coherent remote control and data logging system for the chamber. The CompactRIO consists of a real-time communication module with Gigabit Ethernet network communication, a Field Programmable Gate Array (FPGA) backplane, and four slots for plug-and-play modules to customize the input and output capabilities of the unit to specific experimental needs. Each

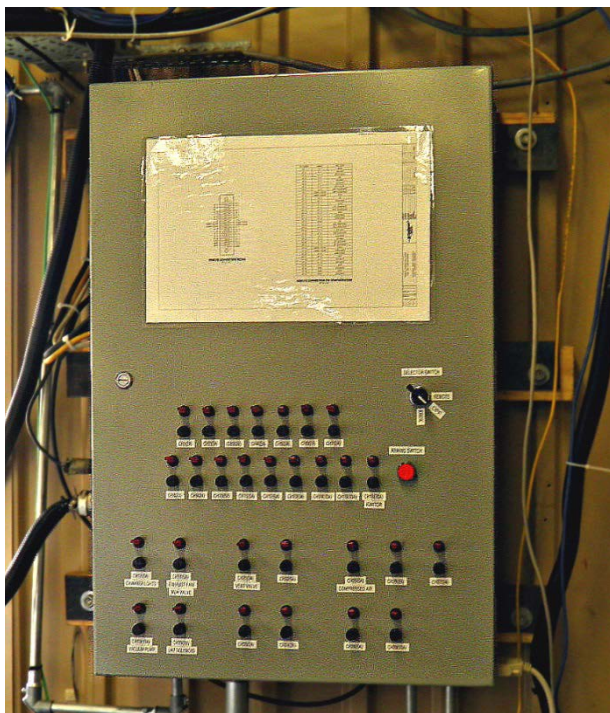


Figure 3: An image of the control box for local control and monitoring of the chamber. The control box also provides an interface for remote communication.

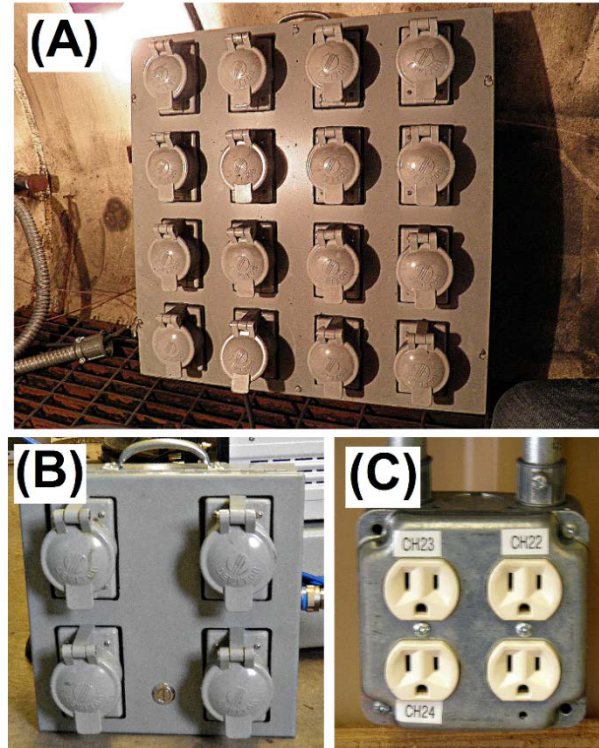


Figure 4: (A) The sixteen-channel trigger box located inside the chamber during experiments; (B) the four-channel "Quad Box" located underneath, but outside, the chamber; and (C) the three channel external power circuit located directly underneath the control box mounted next to the chamber.

module communicates with the real-time communication module through the FPGA backplane. The entire unit, including up to four modules and the FPGA backplane, was programmed using the LabVIEW development environment (LabVIEW 2012 Full, Real-Time Module, FPGA Module, and Application Builder, National Instruments, Inc, Austin, Texas, USA). The real-time communication module acts a server, which can communicate with any number of clients through a Local Area Network (LAN) and its 10/100/1000 Mb sec⁻¹ integrated network interface port. Custom client software was also written in LabVIEW to provide a remote mode interface to the chamber functions through the CompactRIO. Figure 5 shows an image of the four-slot CompactRIO external to the chamber and mounted on the wall next to the chamber control box.

A 32-channel digital TTL (5V) module (NI 9403, National Instruments, Inc., Austin, Texas, USA) was placed in the first slot of the CompactRIO and a 32-channel ribbon cable terminated with female DB32 connectors is used to connect the CompactRIO to the control box. Through this connection, the CompactRIO is able to externally activate and deactivate chamber functions and power channels during experiments when the mode selector switch is set to "Remote".

A Gigabit LAN was implemented to provide remote communication with the chamber, equipment, and the CompactRIO in the chamber building (CBD Building 310) to the control room (CBD Building 312) and command station. In the chamber room, a Gigabit-enabled, eight-port switch (Prosafe GS108, Netgear, San Jose, California, USA) was mounted on the wall next to the four-slot CompactRIO and chamber control box. The CompactRIO was connected to the switch

Table 1: Pin assignments for the DB32 connector on the control box to remotely activate and deactivate chamber functions and channels.

Pin	Chamber Function or Channel
1	16-Channel Trigger Box 1
2	16-Channel Trigger Box 2
3	16-Channel Trigger Box 3
4	16-Channel Trigger Box 4
5	16-Channel Trigger Box 5
6	16-Channel Trigger Box 6
7	16-Channel Trigger Box 7
8	16-Channel Trigger Box 8
9	16-Channel Trigger Box 9
10	16-Channel Trigger Box 10
11	16-Channel Trigger Box 11
12	16-Channel Trigger Box 12
13	16-Channel Trigger Box 13
14	16-Channel Trigger Box 14
15	16-Channel Trigger Box 15
16	16-Channel Trigger Box 16
17	Chamber Lights
18	Exhaust Fan
19	Vacuum Pump
20	Nitrogen
21	Vent
22	External Power Circuit 1
23	External Power Circuit 2
24	External Power Circuit 3
25	Compressed Air
26	Quad Box 1
27	Quad Box 2
28	Quad Box 3
29	Quad Box 4
30	Unused
31	Unused
32	Unused

with a 30 cm (~1.0 ft) Cat6 Ethernet cable to minimize long cables that could cause trips or entanglements with other equipment and connections. Two ~15 m (50 ft) Cat6 Ethernet cables were connected to the eight-port switch and routed to the two RJ45 bulkhead connectors on Port 4 of the chamber. Independent, Gigabit network-enabled equipment and instrumentation placed inside the chamber can be connected to the LAN through the bulkhead connectors inside the chamber on Port 4. A ~45 m (150 ft) Cat6 Ethernet cable was installed to connect the switch in the chamber building with an identical eight-port Gigabit network switch in the control room

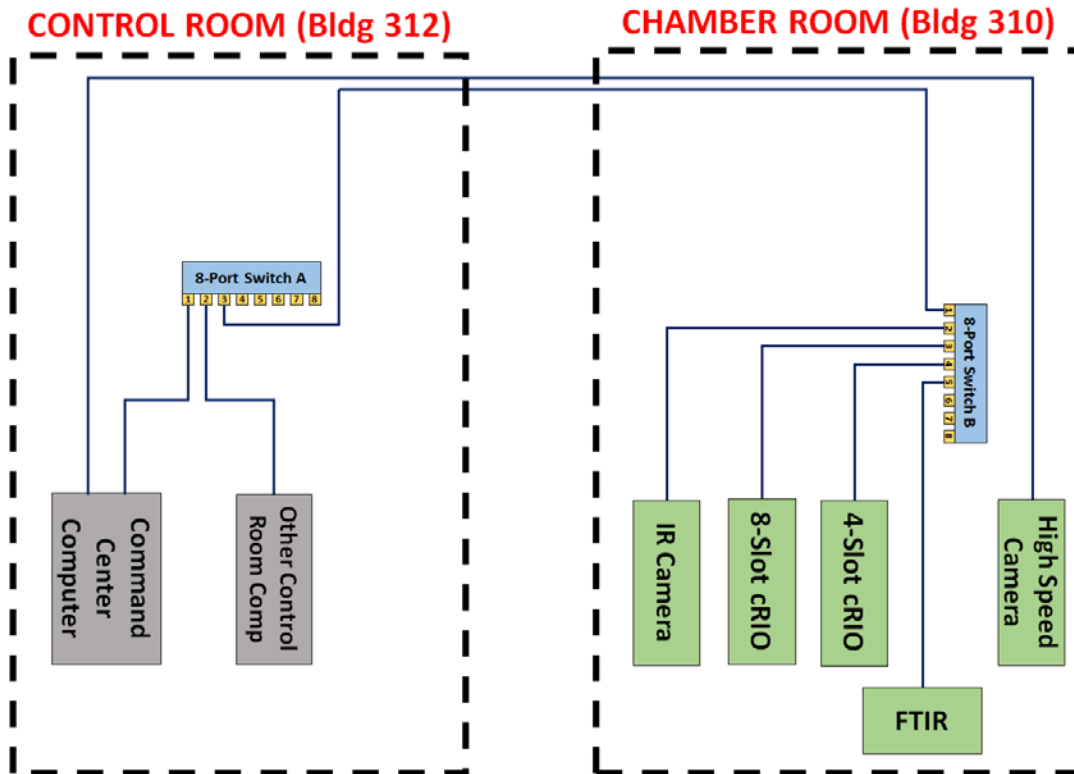


Figure 6: The cabling and hardware connections that make up the Gigabit-enabled Local Area Network for remote chamber control at CBD.

computer was capable of output to six monitors via its two graphics cards, one monitor was eventually used to display the live video feeds from the low resolution, closed circuit chamber video cameras on a separate, older computer (labeled “Other Control Room Comp” in Figure 6) because the drivers for the closed circuit interface board were not Windows 7 or 64-bit compatible. The older computer was running 32-bit Windows XP SP3 and was previously implemented as the chamber room camera controller. The six monitors were mounted on a multiple monitor support that was bolted to an available metal workbench with a shelf underneath for the two computers. The computers, monitors, support, and workbench constituted the remote chamber command station in the control room for the chamber and is shown in Figure 7.

The operating system (Windows 7 64-Bit Ultimate, Microsoft, Inc., Redmond, Washington, USA) was installed on the 128 GB Solid State Drive (SSD), while the two 1 TB Hard Disk Drives (HDDs) were combined into a RAID1 configuration as a minimally implemented, local backup and redundancy strategy to store data files from experiments. Two external, USB 3.0 external hard drives were used to transfer data files from the HDD array and provide a remote backup of the data files from experiments.

Originally it was believed the data from the CompactRIO and other instrumentation could be collected on the Gigabit-enabled LAN through a single connection to the command station computer. However, during setup and installation of new instrumentation, such as high speed

Table 2: A parts list for the custom desktop computer used at the command station in the control room to remotely control and monitor chamber and experimental conditions, respectively.

Part Number	Description	Manufacturer	Supplier
FX-8120	8-core 64-bit 3.1 GHz Processor	AMD	Newegg.com
Sabertooth 990 FX BIOS	AM3+ Socket Motherboard	ASUS	Newegg.com
GeForce GTX 550 Ti	1 GB 2-Channel Graphics Card	Nvidia	Newegg.com
FinePro 2450	256 MB 4-Channel Graphics Card	ATI Technologies	Newegg.com
SSD 840 PRO Series	128 GB Solid State Drive	Samsung	Newegg.com
WD10EZEX	1 TB 7200 RPM Hard Disk Drive	Western Digital	Newegg.com
WD10EZEX	1 TB 7200 RPM Hard Disk Drive	Western Digital	Newegg.com
1x2 Mirror/RAID1	Redundant Array of Independent Disks (RAID) SCSI Disk Device	AMD	Newegg.com
F3-1600C9D- 16GSR	16 GB Memory	GSkill	Newegg.com
DRW-24B1ST	Read/Write DVD drive	ASUS	Newegg.com
EXPI9301CTBLK	10/100/1000Mbps Network Adapter	Intel	Newegg.com
EXPI9301CTBLK	10/100/1000Mbps Network Adapter	Intel	Newegg.com

cameras and an upgraded FTIR, communication connections from some instrumentation required a dedicated cable and network interface card to work properly and reliably. Thus, two additional network interface cards (NICs) were added to the command station computer for a total of three dedicated NICs. The integrated network interface on the motherboard of the custom-built desktop computer was used for communication with the CompactRIO on the Gigabit-enabled LAN, while the two additional NICs were used for instrumentation requiring a dedicated communication interface.

3.2 Chamber Cameras

After upgrading the chamber control box, adding the CompactRIO for enabling remote chamber control, implementing a Gigabit-enabled LAN, and creating a custom command station in the control room, various instrumentation upgrades were completed before conducting experiments on cell-to-cell failure propagation in large format batteries. The first significant instrumentation improvement was adding an Infrared (IR) Camera (A300, FLIR Systems, Inc., Meer, Belgium) and two high speed cameras (HiSpec 1, Fastec Imaging, San Diego, CA, USA). All the cameras were GigE Vision compatible, so they could be connected to the Gigabit-enabled LAN or directly to the

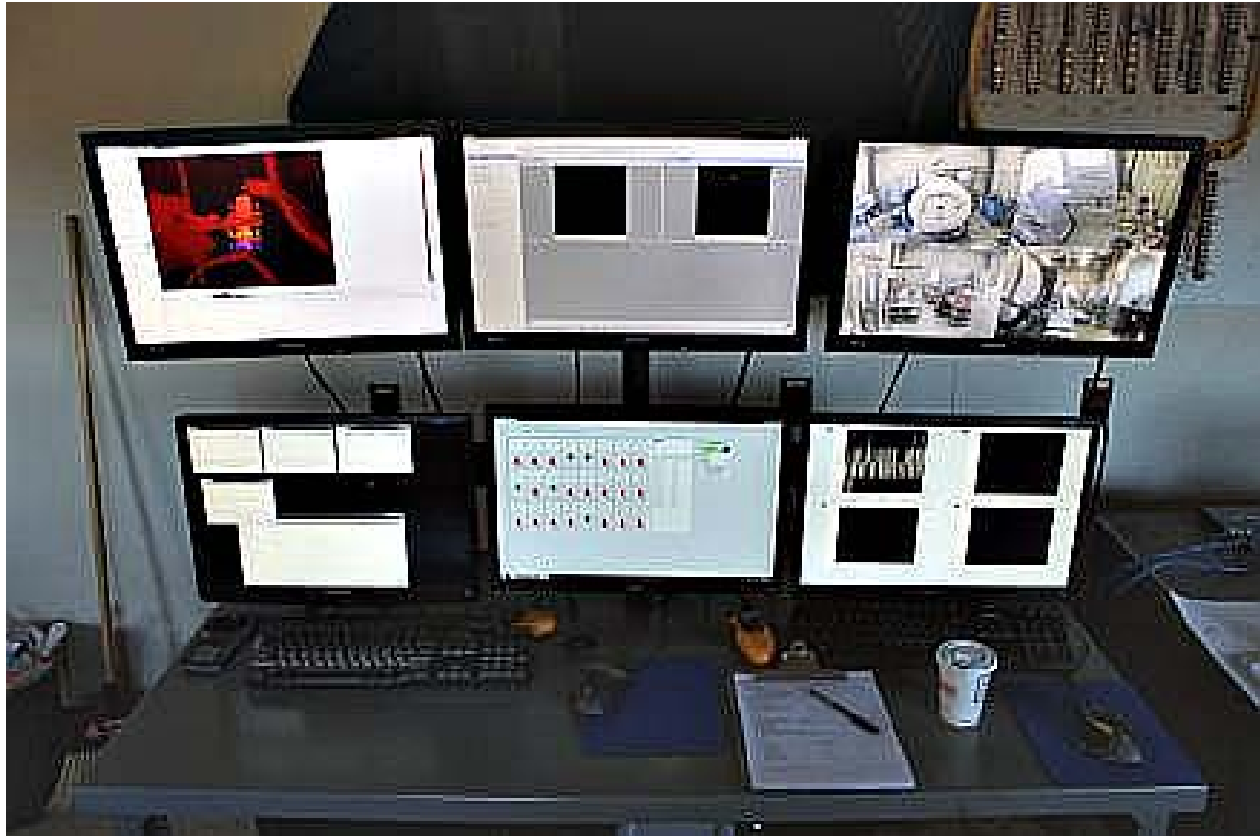


Figure 7: An image of the remote chamber command station in the control room, which is comprised of two desktop computers, six monitors, and a monitor mounting system bolted to a metal workbench.

command station computer's secondary and tertiary NICs. The IR camera and one of the high speed cameras were each put into separate protective enclosures and placed inside the chamber.

The in-chamber cameras, mounted inside their protective enclosures, were placed on lab jack stages to facilitate positioning so their fields of view were centered on the device under test (DUT) in an experiment. Figure 8 shows the locations of the two cameras inside the chamber during an experiment relative to the DUT.

The second high speed camera was to be mounted on the outside of the chamber and in position to view the experiments through one of two port lenses on the chamber. However, a suitable lens and mounting bracket were not available and the second high speed camera was never implemented for the experiments. Installing the second high speed camera is a priority for conducting future experiments.

The IR camera was mounted in a protective enclosure affixed with a ZnSe window (50mm dia. x 2mm thick, 3-12 μ m coating, Edmund Optics, Barrington, NJ, USA), which is transparent to IR light. A power supply cable and Cat6 Ethernet cable was fed through the protective enclosure and connected to the camera. The feed through for the cables was sealed with duct tape to prevent damage to the camera from various harmful fluids that could be expelled during a cell failure. The high speed camera was mounted in a similar protective enclosure but with a soda

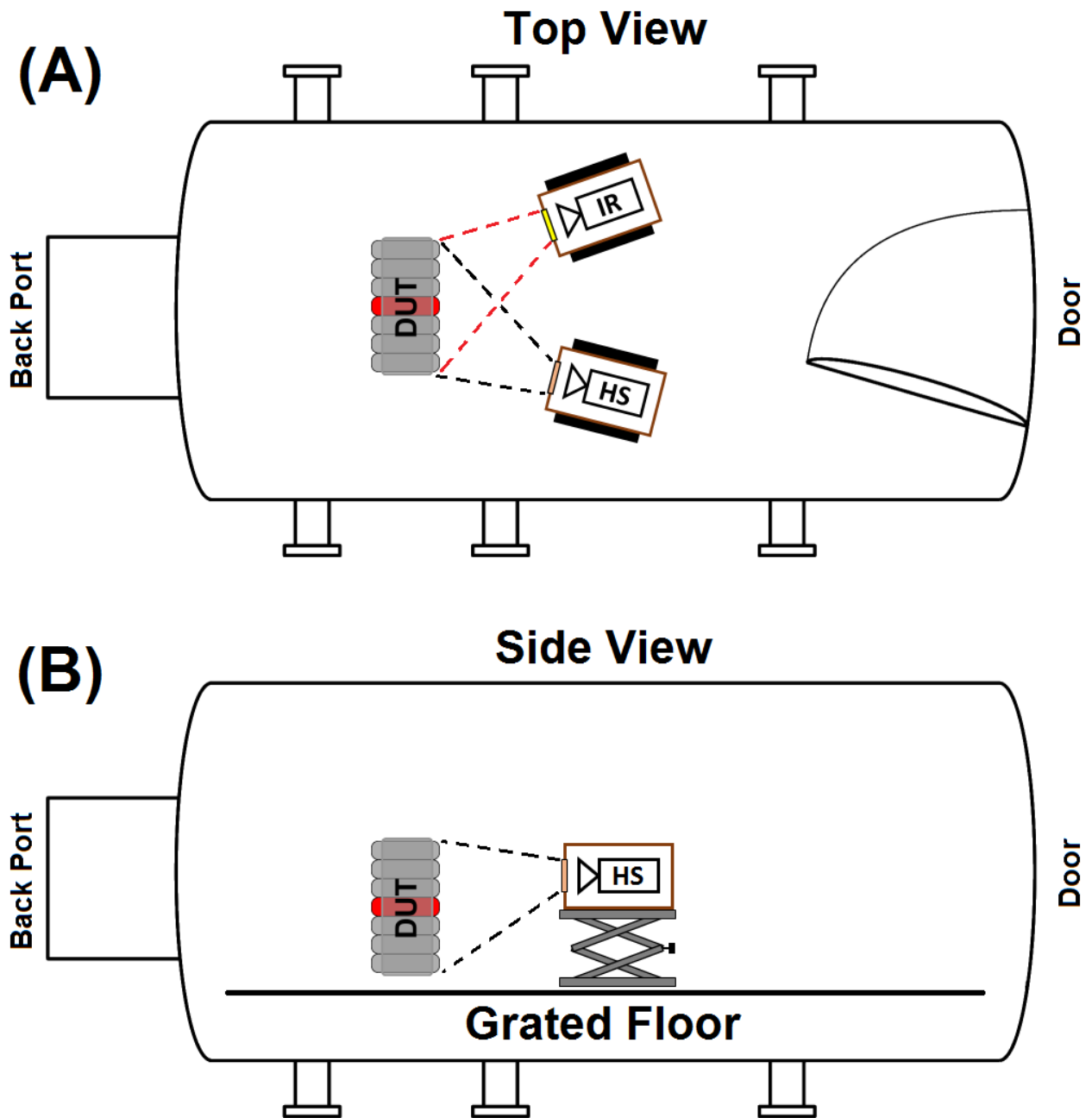


Figure 8: (A) Top and (B) side view diagrams of the IR camera and high speed (HS) camera positions inside the chamber during an experiment. Both cameras were placed in protective enclosures and jab jacks were used to facilitate manual angle, pan, and tilt positioning relative to the device under test (DUT).

lime glass window instead of the ZnSe IR-compatible window. A zoom lens (Nikkor 28mm f/2.8D, Nikon Inc., Melville, NY, USA) was attached to the high speed camera to maximize the field of view. A power supply cable and Cat6 Ethernet cable were connected to the high speed camera and sealed with duct tape, similarly to the IR camera enclosure configuration. The IR camera contained a built-in optical system that included an auto-focus feature that could be enabled remotely through the IR camera software, so no additional optics were implemented for the IR

camera. Figure 9 shows images of the IR camera and high speed camera mounted in their enclosures.

The power cables for both cameras were connected to a power strip inside the chamber that was *not* connected to the trigger box, but rather to an external, always-on power channel through the plate on Port 3 of the chamber. The cameras were originally connected to the sixteen-channel trigger box inside the chamber (Figure 4A), but during dry runs and debugging of the instrumentation and upgraded chamber control system, all the trigger box channels would be deactivated causing the cameras to power cycle. According to the documentation for the cameras, abrupt power failure may cause permanent damage to both types of cameras. Therefore, an always-on power source, regardless of the remote chamber control system state, was provided for the cameras.

Initially, there were concerns about the cameras overheating since they were operating in closed, low-volume environments inside their respective enclosures. In an attempt to mitigate this potential issue, 1/4 in. Swagelok™ bulkhead tube connectors were mounted on each enclosure. Plastic tubing (1/8 in. ID, 1/4 in. OD) was plumbed from the vacuum pump connection inside the chamber through the plate on Port 3 to both camera enclosures. The vacuum pump was used to draw ambient air from the room into the enclosures to convectively cool the cameras. After some initial experiments, it was determined that there was no significant temperature rise inside the enclosures (monitored by embedded temperature sensors in the two cameras) regardless of whether or not the forced air cooling mechanism was activated. The air cooling system was



Figure 9: The IR and high speed cameras mounted in their protective enclosures. The IR camera enclosure (right) was affixed with a ZnSe window which is transparent to IR light, and the high speed camera enclosure (left) contained a soda lime glass window. Both cameras inside their respective enclosures were placed inside the chamber during experiments.

therefore removed and the bulkheads capped to prevent harmful fluids from entering the enclosures. However, to ensure safe operation of all instrumentation and equipment, the camera temperatures were still actively monitored during testing.

Through initial dry runs of the instrumentation, it was discovered that the high speed camera needed a dedicated communication cable to the command station computer, unlike the IR camera which was simply connected to the Gigabit-enabled LAN through the CompactRIO. A second ~45 m (150 ft) Cat6 Ethernet cable was run from the chamber to the command station computer located in the control room. The cable was not connected to any of the Gigabit-enabled LAN switches or network; instead, it was connected directly to the camera and the secondary NIC on the command station computer. The high speed camera is GigE Vision compatible, but packet loss issues (dropped frames) would arise if it shared communication with other cameras and devices. According to the manufacturer's (Fastec Imaging) limited documentation, each high speed camera being used simultaneously should have its own communication cable with a dedicated NIC on the computer for optimal performance and utility, while the software is capable of controlling, displaying, and encoding high speed video feeds for up to four individual cameras. Therefore, in the future it will be necessary for additional NICs (or a single NIC with multiple GigE ports) to be implemented in the command station computer to ensure numerous high speed cameras can be effectively operated simultaneously during tests.

Both cameras came with software to control, display, and encode video. The IR camera software (ExaminIR, FLIR Systems, Inc., Meer, Belgium) included functionality for placing cursors on the live image for real-time temperature measurements, graphing cursor values versus time, and changing the color palette. Both camera software programs included a wide-range of parameters and settings to optimize performance for specific applications. The optimized parameters for both cameras were determined experimentally during dry run events and the ideal values are shown in Table 3 and Table 4 for the IR and high speed cameras, respectively.

The high speed camera has an internal frame buffer that can store up to 13099 frames at a time. Consequently, at 500 fps only the most recent 26.2 seconds of video was actively saved, and it was important during experiments to stop recording on the high speed camera after an event occurred in order to preserve the video capture of the event. Both camera software programs allowed saved videos to be exported. The ideal work flow, which was determined experimentally, was to export each frame from the saved high speed camera video as Tagged

Table 3: Experimentally-optimized parameters for the IR camera.

Parameter	Value
Frame Rate	1 fps
Record to Disk	Checked
Start/Stop Recording	Checked
Limit Record Rate	2 Hz
Display Images While Recording	Checked
Limit Display to	2 Hz

Table 4: Experimentally-optimized parameters for the high speed camera.

Parameter	Value
Frame Rate	500 fps
Shutter Speed	1994 μ s
Blacklevel	150
Digital Gain	2.5
Enable Quad Mode	Checked
Dynamic Range Adjustment	75
Display Rate	25 fps
Playback	30 fps
Check Camera Temperature	Checked
Record Mode	Ring

Image File Format (TIFF) files and use the public domain software ImageJ [National Institutes of Health (NIH), Research Services Branch (RSB)] to crop and compile the individual frames into a standalone Audio-Video Interleave (AVI) file that could be replayed on any device without the need for the camera control software. In order to obtain temperature information and export standalone video files from the IR camera recordings, the ExaminIR software could be used directly.

3.3 Real-Time Gas Analyzers and In-Situ FTIR

Chemical analysis of gas composition during testing was performed using two different types of instrumentation: two non-dispersive, infrared real-time gas analyzers (ZRE, California Analytical Instruments, Orange, California, USA) and an in-situ Fourier Transform Infrared (FTIR) Spectrometer (I-Series, MIDAC Corporation, Westfield, Massachusetts, USA). The two real-time gas analyzers, which are shown in Figure 10A, were calibrated to monitor concentrations of

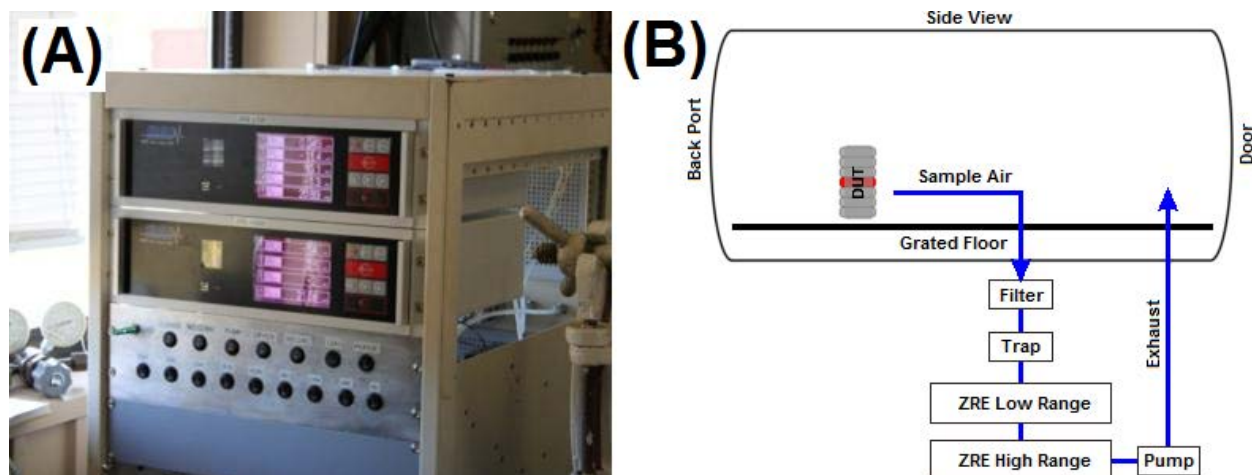


Figure 10: (A) Image of the two ZRE real-time gas analyzers used during testing; (B) diagram of the configuration for the ZREs with the chamber. Chamber air was draw out of the plumbing bulkhead, Port 3, analyzed by each ZRE, then pumped back into the chamber to maintain an overall closed system.

Table 5: Detectable gases and concentration ranges monitored by the two ZRE real-time gas analyzers (Low Range and High Range).

Gas	Molecular Formula	Low Range ZRE	High Range ZRE
Carbon dioxide	CO ₂	0-5%	N/A
Carbon monoxide	CO	0-200 ppm	0-1000 ppm
Sulfur dioxide	SO ₂	0-500 ppm	0-1000 ppm
Oxygen	O ₂	0-25% (paramagnetic)	0-25% (fuel cell)
Methane	CH ₄	N/A	0-500 ppm

carbon dioxide (CO₂), carbon monoxide (CO), sulfur dioxide (SO₂), oxygen (O₂), and methane (CH₄) in varying concentrations. One ZRE was used to measure low ranges of concentrations (along with a paramagnetic oxygen sensor) while the second ZRE was used for high ranges (with a fuel cell-based oxygen sensor). Table 5 lists the gases and concentration ranges for both ZREs.

Data logging with the two ZREs was performed using 4-20 mA output signals interfaced directly with the four-slot CompactRIO in real-time during testing. Chamber air was drawn from the plumbing bulkhead, Port 3 (see Figure 1B and Figure 2) into both ZREs, then pumped back into the chamber to maintain an overall closed system. Figure 10B shows a diagram of the configuration for the ZREs in combination with the chamber during testing.

In-situ FTIR was performed during tests to further identify gas and liquid species released from batteries during failure events. The FTIR Spectrometer was calibrated with a 0.5 cm⁻¹ spectral resolution and a 3 second time resolution. Figure 11 shows an image of the FTIR highlighting the direction of the beam path (Figure 11A), along with the hardware inside the chamber (Figure 11B). The beam was directed into the chamber via Port 2 and returned to the spectrometer via Port 1 (see Figure 1B for port identification). Inside the chamber, the beam was directed through two pressure-tight boxes containing IR-transmitting windows spaced 40 cm apart. Analysis software for the FTIR

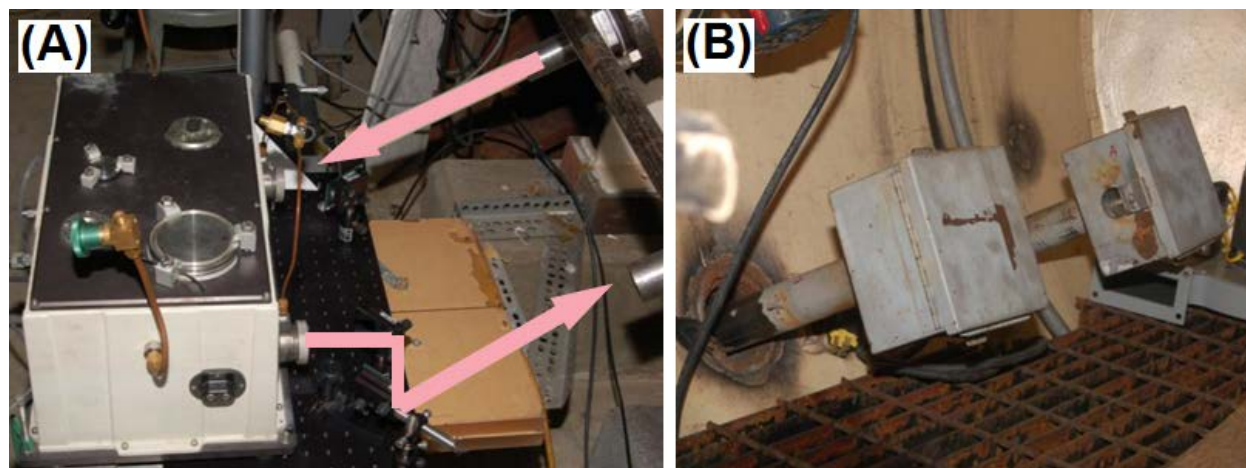


Figure 11: (A) Image of the in-situ Fourier Transform Infrared Spectrometer sitting outside the chamber illustrating the beam path direction going into Port 2 and returning to the spectrometer via Port 1 (see Figure 1B for port identification); (B) internal hardware directing beam path through pressure-tight boxes with IR windows that are spaced 40 cm apart.

was used to continuously monitor gaseous combustion products (e.g. CO and CO₂) as well as liquid electrolyte species (e.g. dimethyl carbonate and ethylene carbonate) in real-time.

3.4 Surrogate Cells

Surrogate cells were designed and fabricated to mimic the thermal behavior of active lithium-ion battery cells without the danger or complexity of active components. Through implementation of surrogate cells, repercussions of single active cell failure events could be observed and studied without the complexity or hazard of multiple events occurring simultaneously or in a cascading effect. A diagram of the surrogate cells is shown in Figure 12. Cells consisted of a nickel-plated steel 18650-type casing (18mm [0.7"] diameter, 65mm [2.6"] length), a grooved aluminum core, and a crimped-on cap similar to the style of active 18650 cells. Three thermocouples were inserted into each of the grooves (and the center hole) in the aluminum core to measure temperatures at different locations in the surrogate cell, all varying distances from the active cell failure event (and/or surrogate heater cell) which was producing heat. This enabled the potential to observe heat propagation as energy flowed spatially into and through the surrogate cells during a failure test. Some of the cells were also instrumented with one or two heat flux gauges on the surface of the case, which were designed and fabricated in-house and consisted of two thin-foil thermocouples separated by a thin insulating layer.

Specially-instrumented surrogate cells with an internal cartridge heater were also fabricated and used in multi-cell packages to induce failure from heat propagation to an active cell, rather than as a result of purely overcharge abuse. Figure 13 shows a diagram of a typical surrogate heater cell design. These cells were nearly identical to the standard surrogate cells shown in Figure 12, but rather than a center-positioned thermocouple, the middle of the aluminum core was

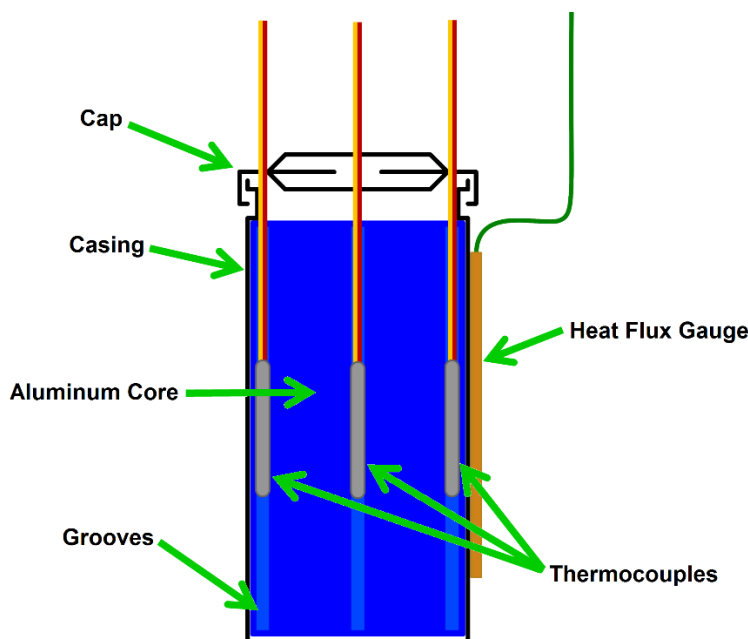


Figure 12: Diagram of fully instrumented surrogate cell, including heat flux gauge, inserted thermocouples, aluminum core with grooves, casing, and crimped-on cap.

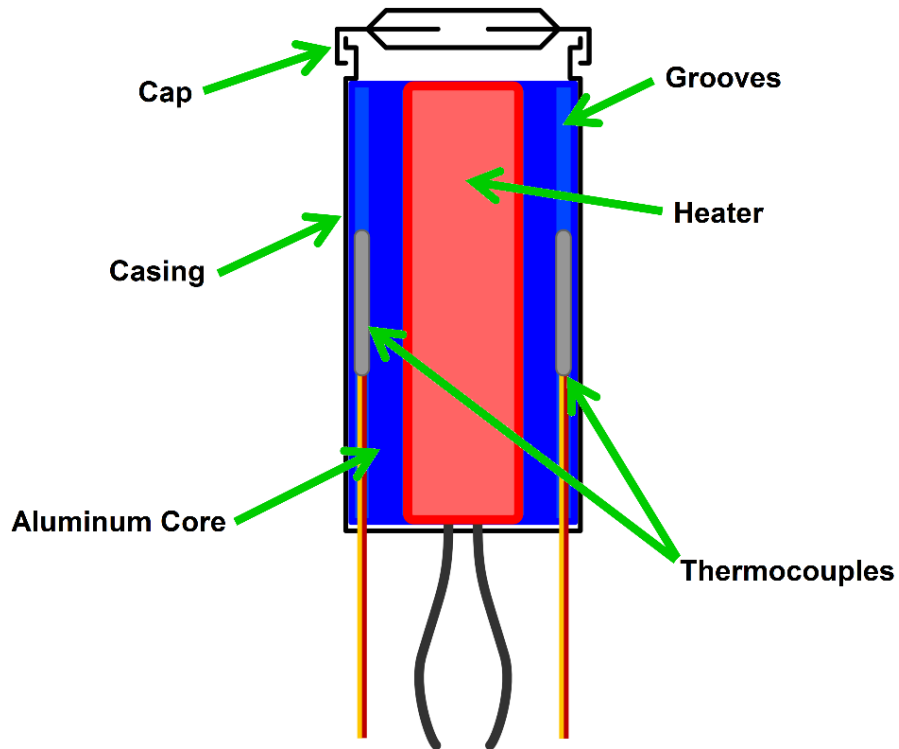


Figure 13: Diagram of fully instrumented surrogate heater cell, including two inserted, side-positioned thermocouples, aluminum core with grooves and hollowed out center with inserted cartridge heater, casing, and crimped-on cap.

hollowed out and a cartridge heater was inserted instead. Otherwise, the design remained the same with the nickel-plated steel 18650-type casing, crimped-on cap, aluminum core with grooves, and two side-positioned thermocouples.

3.5 Multiple Cell Packaging

A hexagonal-shaped cluster of cells was used for multiple cell packaging tests, including an active cell, a surrogate heater cell, surrogate cells, and heat flux gauges. Figure 14A shows a diagram identifying each part of the typical hexagonal cluster setup, and Figure 14B shows the labeled locations and positions of each individual thermocouple and both heat flux gauges on either side of the central active cell. In all, there were 21 temperatures actively measured between all thermocouples and both heat flux gauges during any given test. The hexagonal package was put together using hot glue to keep the cells together in the desired shape, and then the entire cluster was wrapped and tightened in place using a large hose clamp. The heat flux gauges, as previously mentioned, were designed and fabricated in-house and consisted of two thin-foil thermocouples separated by a thin insulating layer.

A second, eight-slot CompactRIO (cRIO-9014, National Instruments, Inc., Austin, Texas, USA) was added to enable further monitoring of thermocouple signals inside the chamber. This CompactRIO was mounted inside a separate enclosure along with a five-port Gigabit network switch (Prosafe GS105, Netgear, San Jose, California, USA) and power supply, and the enclosure

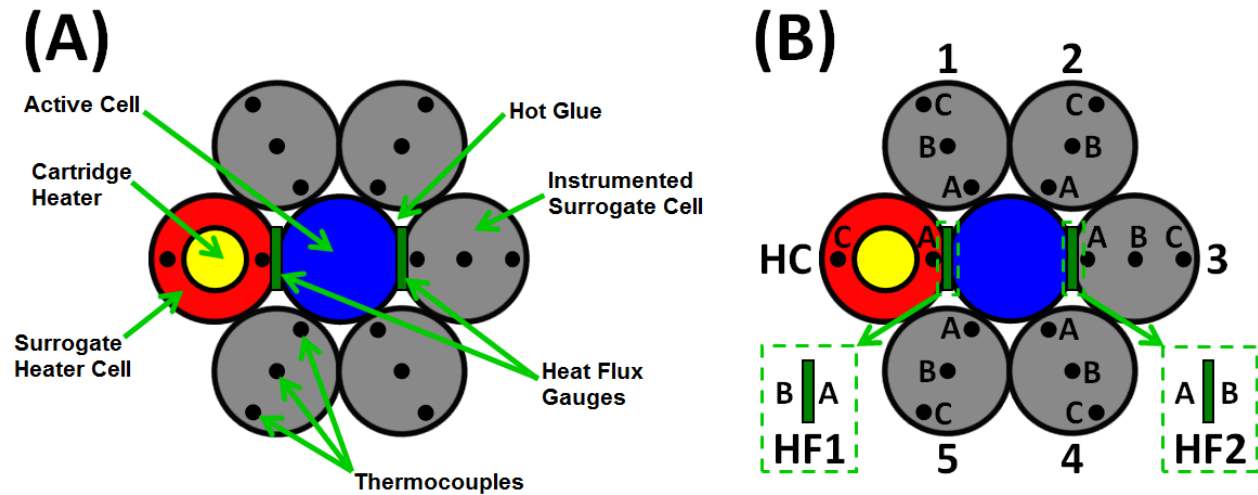


Figure 14: (A) Labeled diagram of typical hexagonal package of 18650 cells used for lithium-ion battery failure tests, which included a single active cell, a surrogate heater cell, five surrogate cells, and two heat flux gauges. The cells were hot glued into place and bound together with a hose clamp. (B) Locations and labels for corresponding surrogate cells, surrogate heater cell (HC), and heat flux gauges (HF) by number and letter. A total of 21 temperature measurements were recorded actively including all surrogate cell and surrogate heater cell thermocouples, as well as four temperatures from both heat flux gauges. For all locations and monitored temperatures, 'A' represents the position closest to the active cell, followed by 'B' and 'C' (if applicable) moving away from the active cell.

was placed inside the chamber during tests. Figure 15 shows a picture of the eight-slot CompactRIO, five-port Gigabit network switch, and power supply mounted on a plate in the enclosure. The five-port Gigabit network switch was used for connecting the eight-slot CompactRIO to the command station computer via one of the RJ45 chamber bulkhead connectors installed in Port 4 (see Figure 1B), and also for connecting the IR camera inside the chamber to the LAN. Since one RJ45 chamber bulkhead connector in Port 4, as previously mentioned, was needed for a direct connection from the command station computer to the high speed camera, only one Ethernet port remained going into the chamber. Therefore, the need arose for the additional five-port Gigabit network switch to ensure proper communication between the command station computer and all desired instrumentation.

In addition to temperature monitoring via the two CompactRIOs, active cell voltage was monitored using a channel in the eight-slot CompactRIO. Cell voltage was also controlled using an 18V-10A power supply (AMETEK, Sorensen XPH Series 18V 10A, San Diego, CA, USA) to initiate overcharge abuse tests. The power supply, which is pictured in Figure 16, was connected to the active cell via one of the BNC bulkhead connectors installed in Port 4 of the chamber. In all cases, simple overcharge abuse resulted in significant heat generation from the active cell, but not complete thermal runaway or a credible failure event. For this reason, surrogate heater cells were implemented in the hexagonal cell packages so that thermal abuse could ensure a failure event would eventually take place. The cartridge heater inside the surrogate heater cells was controlled using a Variable Transformer (3PN1010B 140V 10A output, Staco Energy Products Co., Miamisburg, Ohio, USA) and it was modulated using one of the outlets on the sixteen-channel trigger box to allow precise command over when to turn the heating process on and off.

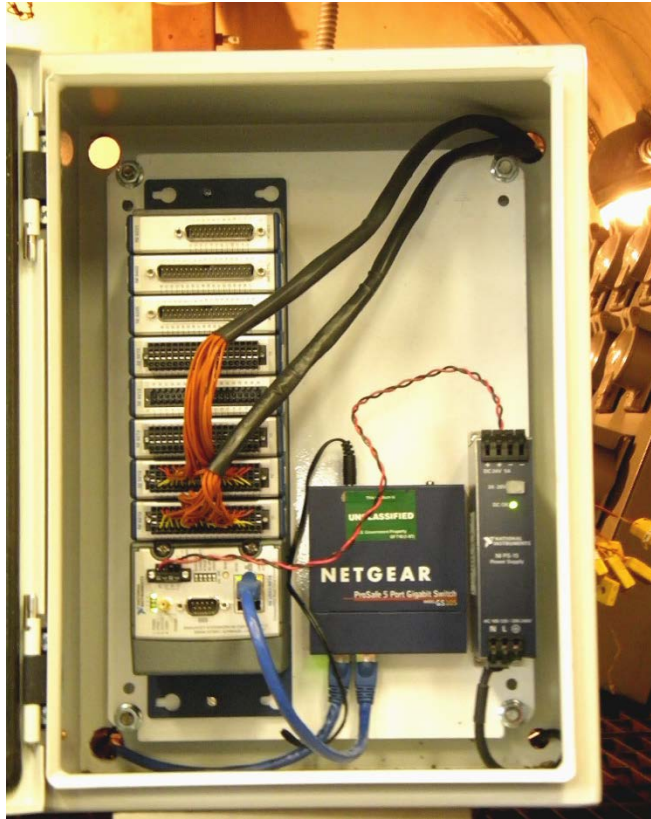


Figure 15: Picture showing the eight-slot CompactRIO, five-port Gigabit network switch, and power supply mounted onto a plate inside an enclosure. Port holes for attaching thermocouples and network cables to the various components were drilled into the back of the enclosure and sealed with duct tape prior to testing to prevent harmful fluids from potentially damaging the equipment.



Figure 16: An image of the power supply used to overcharge the cells.

Overcharge abuse alone was not sufficient to induce a failure event because of safety features within the battery, including a positive temperature coefficient (PTC) disk and current interrupt device (CID) [10,18]. Figure 17 shows a cutaway view of the internal components of a typical 18650 lithium-ion battery including these safety features. Under normal operation (Figure 17A), a thin metal tab pressing against a small button (constituting the CID) ensures electrical contact between the cathode internally and the cap externally. However, in the event that the battery temperature rises and gases are released which causes an increase in internal pressure (Figure 17B), the metal CID button is forced upwards and loses contact with the thin metal tab, thus opening the circuit and permanently disabling the battery. This irreversible safety feature is coupled with the reversible PTC which is illustrated in Figure 17C. The PTC disk consists of a polymer which is either intrinsically electrically conductive, or is doped with conductive carbon particles to impart additional conductivity. At normal operating temperatures, the crystalline polymer forms a chain of molecules which can shuttle electrons with very low resistance. However, if the battery temperature rises above the polymer's glass transition temperature (T_g , typically around 125°C), the polymer becomes amorphous and no longer conducts electrons, thus opening the circuit temporarily until the battery cools and the polymer can recrystallize. Therefore, the rise in internal temperature from overcharging resulted in one or both of these

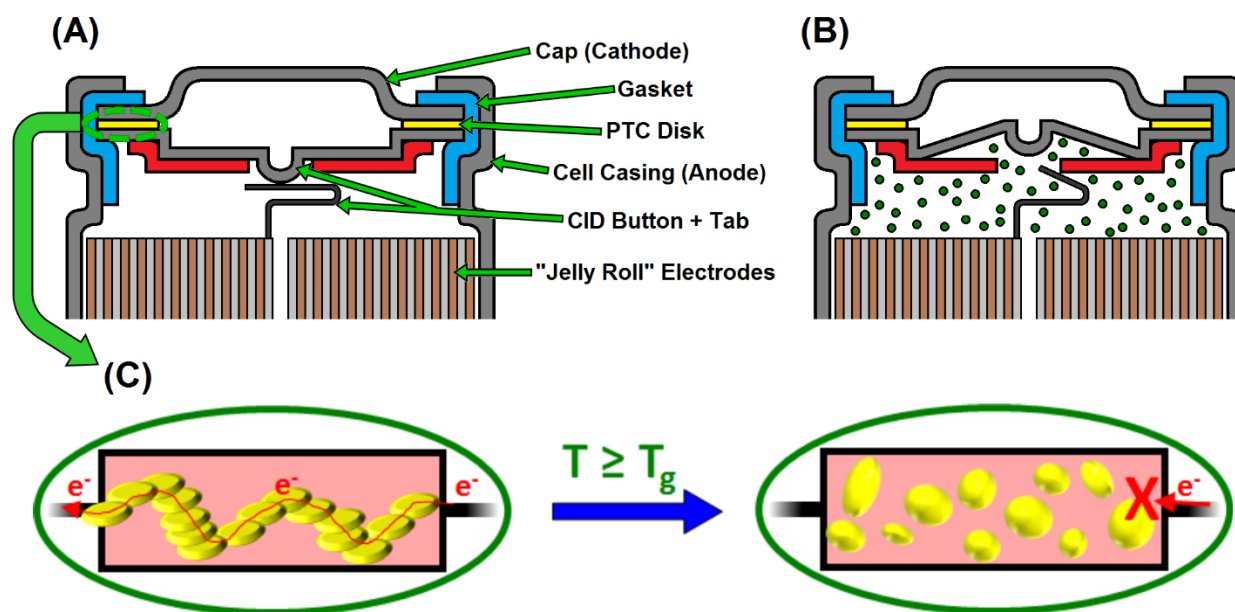


Figure 17: (A) Labeled cutaway view of a typical 18650 lithium-ion battery under normal operating conditions, including the cap (cathode), insulating gasket which separates anode from cathode, cell casing (anode), "jelly roll"-shaped internal electrodes, and two built-in safety devices: the positive temperature coefficient (PTC) disk and current interrupt device (CID). (B) Battery under tripped CID conditions whereby release of gases causes increase in internal pressure forcing metal CID button upwards and eliminating contact with metal tab, thus opening the circuit and effectively "shutting off" the battery permanently. (C) Illustration of operation of PTC device. Disk consists of a polymer which is electrically conductive at ambient temperatures, thus forming a chain of molecules to conduct electrons. Above the glass transition temperature (T_g), however, the polymer becomes amorphous and can no longer conduct electrons, thus opening the circuit until the battery cools and the polymer can recrystallize. Battery cutaway adapted from [19].

safety features being tripped, thus opening the circuit and preventing further abuse from overcharge. For this reason it was necessary to utilize the cartridge heater as a secondary means for raising battery temperature to induce a credible failure event.

4.0 Results

4.1 Single Cell Failure Event

For all battery failure events studied, the active cell used was an 18650 lithium-ion battery with either LiCoO_2 cathode chemistry (ICR 18650J 2370mAh 3.7V, E-One Moli Energy Corp., Taipei, Taiwan) or LiFePO_4 cathode chemistry (APR18650 1100mAh 3.3V, A123 Systems, Waltham, Massachusetts, USA). First, a single LiCoO_2 standalone battery was tested to observe characteristics of a typical failure event and to ensure the proper functioning of all equipment. A cartridge heater was attached to the battery along with a thermocouple for surface temperature measurements, and the battery was abused to the point of failure. Figure 18 shows IR camera and high speed camera images just before, and during, the failure event. Just prior to

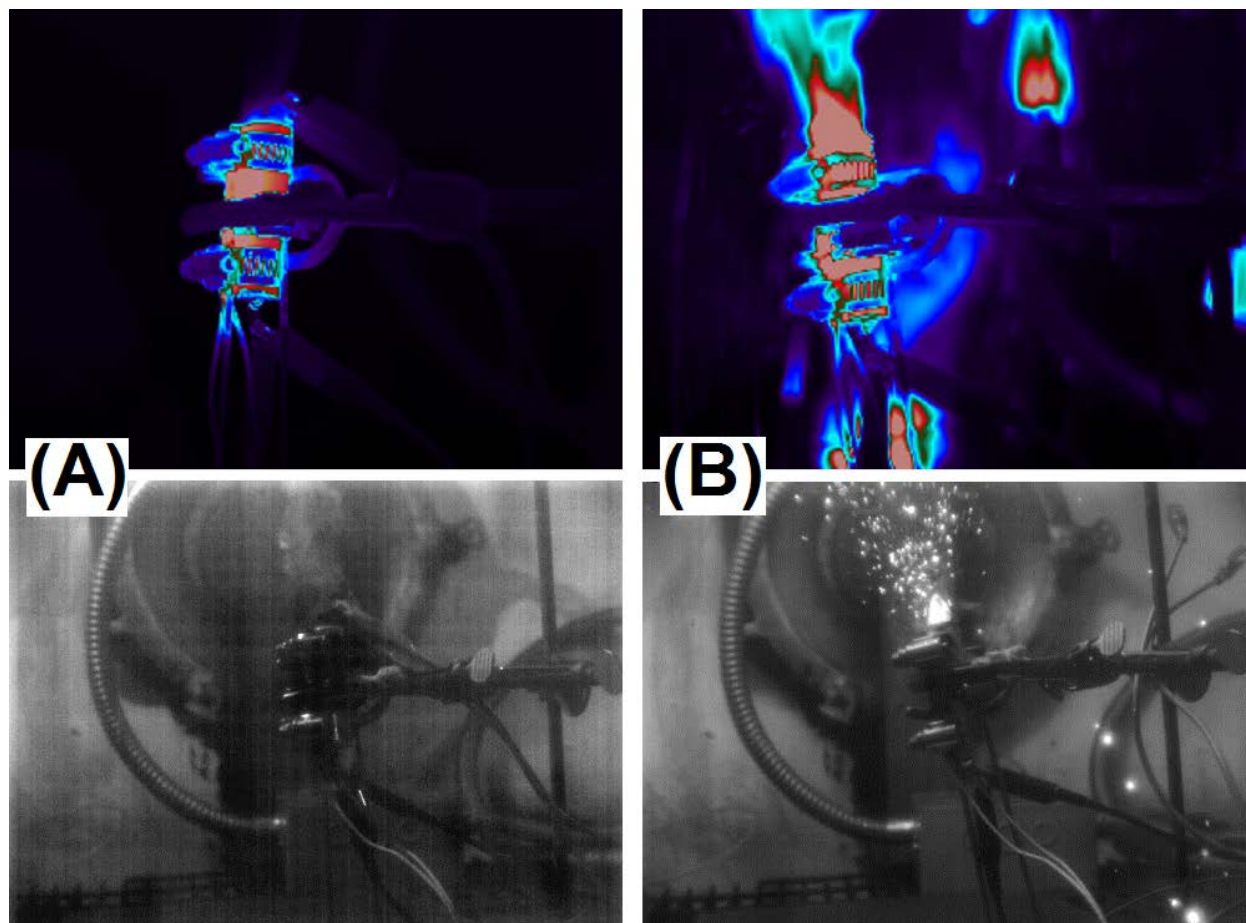


Figure 18: (A) IR camera (top left) and high speed camera (bottom left) frames just before single cell failure event; and (B) IR (top right) and high speed (bottom right) images during failure event. Battery was a LiCoO_2 chemistry 18650 lithium-ion cell, and failure was induced through combination of overcharge followed by external heating.

the event, vapor was seen rising from the top of the battery from the release of internal pressure via venting, and the IR camera showed the battery to be almost uniformly red-hot. The failure event caused sparking and release of hot gases, as well as expulsion of internal and external components. Shortly after the event was finished, the battery began to quickly cool back down.

Figure 19A shows the surface temperature of the battery over time, as well as the battery voltage and heater on/off switch (1=on, 0=off). After a short lag time, the voltage from the power supply was maxed out to 18V, causing a modest increase in battery temperature. At around the 27-minute mark, the voltage was cut off since it was no longer having an effect on the battery temperature (likely due to triggering of the PTC and/or CID) and the heater was turned on, resulting in a dramatic increase in temperature up to the 30-minute mark where the event took place. A spike in temperature to around 492°C corresponded with the failure event, followed by rapid cooling once the event had completed. Including visible venting of gases, the entire event lasted about 40-50 seconds; however, the actual failure event only lasted around 2-3 seconds, as evidenced by the sharp peak seen in Figure 19A.

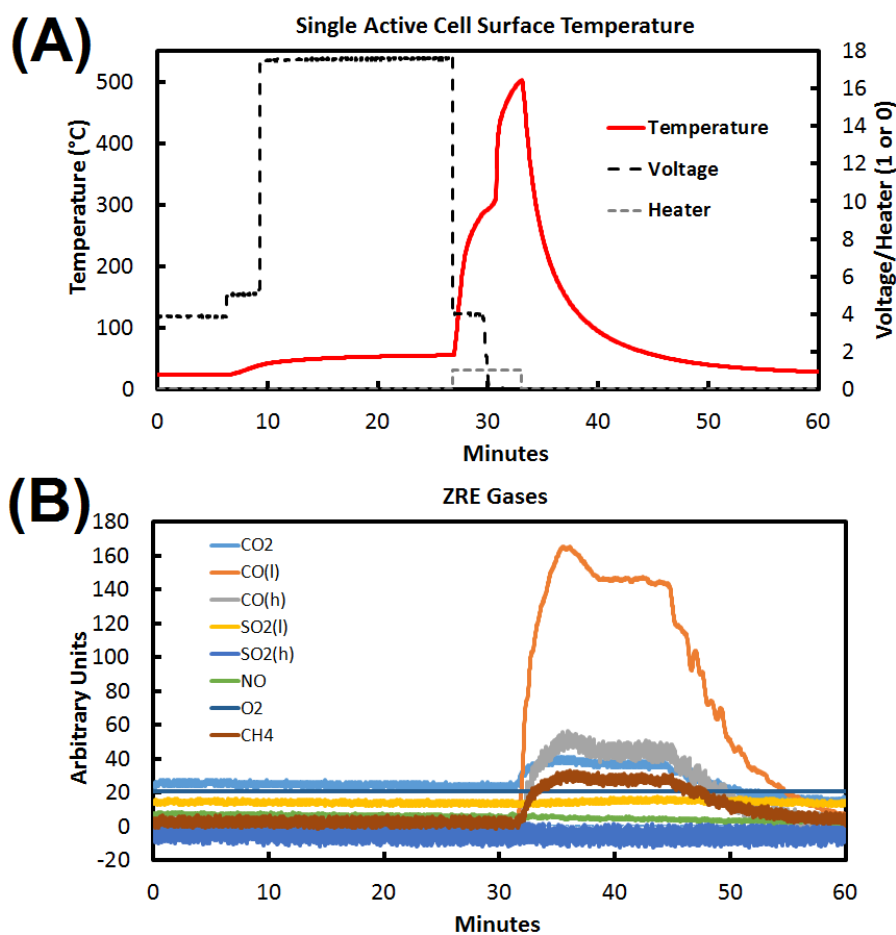


Figure 19: (A) Temperature-time profile for single battery failure event, along with monitored battery voltage and on/off switching of cartridge heater. (B) Gases detected by the two ZRE real-time gas analyzers as a function of time.

Gaseous species released during the failure event were identified using the two ZRE real-time gas analyzers, and time-resolved plots of all species measured are shown in Figure 19B. The most prevalent gases observed were CO, CO₂, and CH₄, with a trace amount of SO₂ also detected. The large ratio of CO to CO₂ makes sense in light of the pressurized conditions inside the battery as it was undergoing failure. As the internal temperature increased, O₂ was formed via release from the LiCoO₂ cathode [20] and/or decomposition of the electrolyte, and combustion started to occur. Since conditions inside the battery were highly pressurized with such a small volume, there was likely a severe deficiency of O₂ compared to all flammable materials, leading to mostly incomplete combustion releasing high levels of CO. However, as shrapnel/gases were then expelled from the battery, ambient O₂ became readily abundant and available leading to more complete combustion, thus accounting for the CO₂ signal seen in Figure 19B. CH₄ likely originated from the decomposition of organic hydrocarbons in the electrolyte (dimethyl carbonate, ethylene carbonate, propylene carbonate). The presence of trace SO₂ was very curious, since no internal components in any of the anode, cathode, separator, or electrolyte supposedly contained any sulfur, according to the specifications provided by the manufacturer. Therefore, it is possible there were either trace impurities of sulfur in one of these components or in the metals comprising the battery, or else an additive not listed by the manufacturer, which was oxidized during the failure event, releasing small quantities of SO₂. Additionally, another explanation for the presence of an SO₂ signal could be cross sensitivity of sensors within the ZREs. The manufacturer literature specifies that SO₂ can be falsely detected at a rate of up to 5% of a positive CH₄ signal, and therefore it is possible there was no SO₂ at all and the signal arose simply as a result of abundant CH₄ expelled during failure.

4.2 Hex Package Cell-to-Cell Failure Events

After observing the single cell failure characteristics, packages of cells in a hex configuration (shown in Figure 14) were constructed and tested. First, to make non-failure observations on heat flow to surrogate cells and energy traveling through the heat flux gauges during overcharge, a LiFePO₄ battery was used as the active cell due to its intrinsic safety compared to LiCoO₂ [21]. Figure 20 shows IR camera images of the setup at the onset of 3A overcharging and after several minutes of heat distribution once the current was removed. These time-lapsed images display how heat is propagated from the center cell outward to the surrounding surrogate cells as its internal temperature rises from an overcharge abuse.

Figure 21 shows temperature- and voltage-time plots, as well as heat flux measurements versus time, for this 3A overcharge abuse (non-failure) test. Since there was no activation of the cartridge heater for this test, only the active cell was producing heat from the center position in the hex package. This explains why a great degree of uniformity was seen in the temperature profiles in Figure 21A. Heat produced from the overcharging active cell propagated radially outward nearly uniformly to the six surrounding surrogates, raising their temperatures to between 47-55°C until around the 51-minute mark. At that time, the voltage steeply dropped down nearly to zero, indicating the triggering of an internal safety feature that opened the circuit and stopped the overcharge. Interestingly, the rate of cooling amongst surrogate cells appeared much slower than the rate of cooling seen in Figure 19A for the single cell after its failure event.

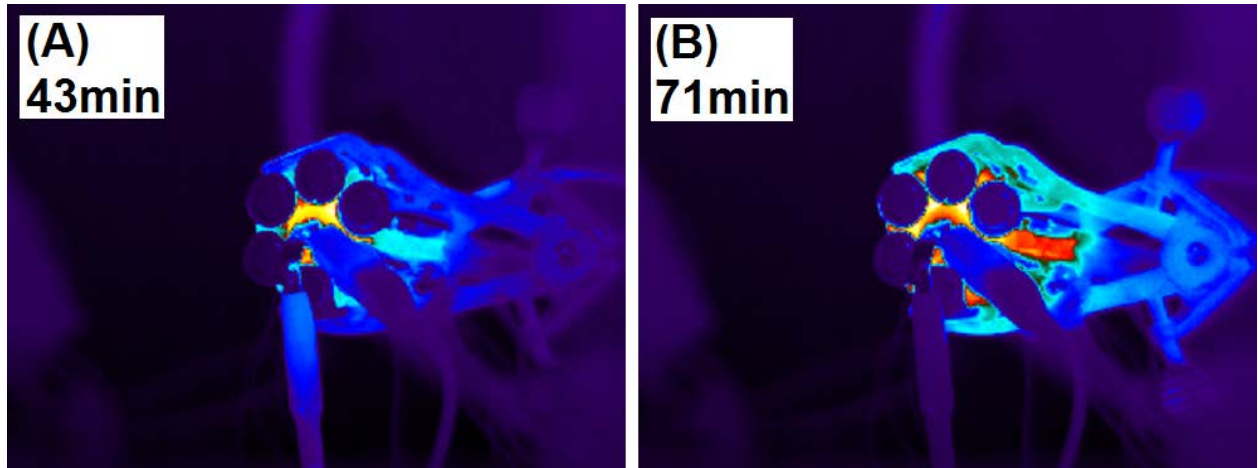


Figure 20: IR camera images of hex package during non-failure overcharge event (A) at the onset of overcharging around the 43-minute mark, and (B) after overcharging was complete around the 71-minute mark. Active cell in the center was LiFePO_4 chemistry; abuse was 3A overcharge test.

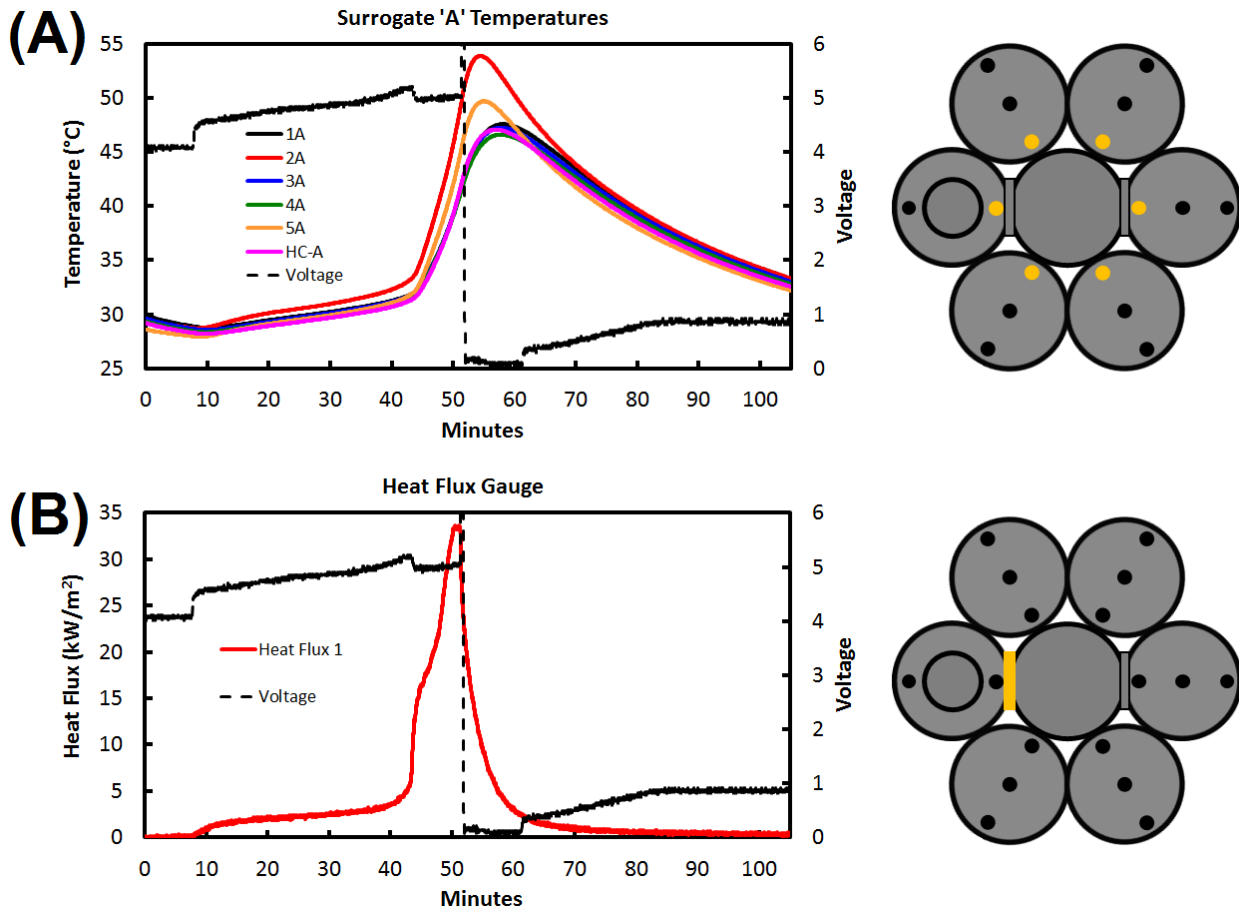


Figure 21: (A) Thermocouple temperature readings and battery voltage versus time for 'A' position thermocouples, along with diagram of hex package with highlighted locations for corresponding temperature readings (see Figure 14 for complete labels and numbering). (B) Heat flux measurement and battery voltage versus time, along with corresponding diagram highlighting location. Data for 3A overcharge abuse (non-failure) test of LiFePO_4 active cell.

This was likely due to the greater overall mass with reduced externally-cooled surface area compared to the single active cell. With the single cell, the entire cylindrical cell casing was exposed to ambient air, which facilitated rapid cooling. However, with the hex package, only about half of the cylindrical cell casings for the surrogate cells were exposed to ambient air for cooling, and virtually none of the center active cell was exposed. This created more interfacial surface area between cells of similar temperatures within the hex package, and without a significant temperature difference the driving force for cell cooling was minimal. In addition, this may also explain why the heat flux seen in Figure 21B dropped off so sharply after the overcharging stopped because heat flux is a function of temperature difference as well.

Next, using LiCoO_2 chemistry for the active cell, two hex package failure tests were performed. Figure 22 shows IR and high speed camera images of the first of these tests (denoted “hex package 1”), and corresponding surrogate cell temperatures, battery voltages, heater on/off controls, and ZRE gas analysis results are shown in Figure 23. As illustrated in Figure 23, after

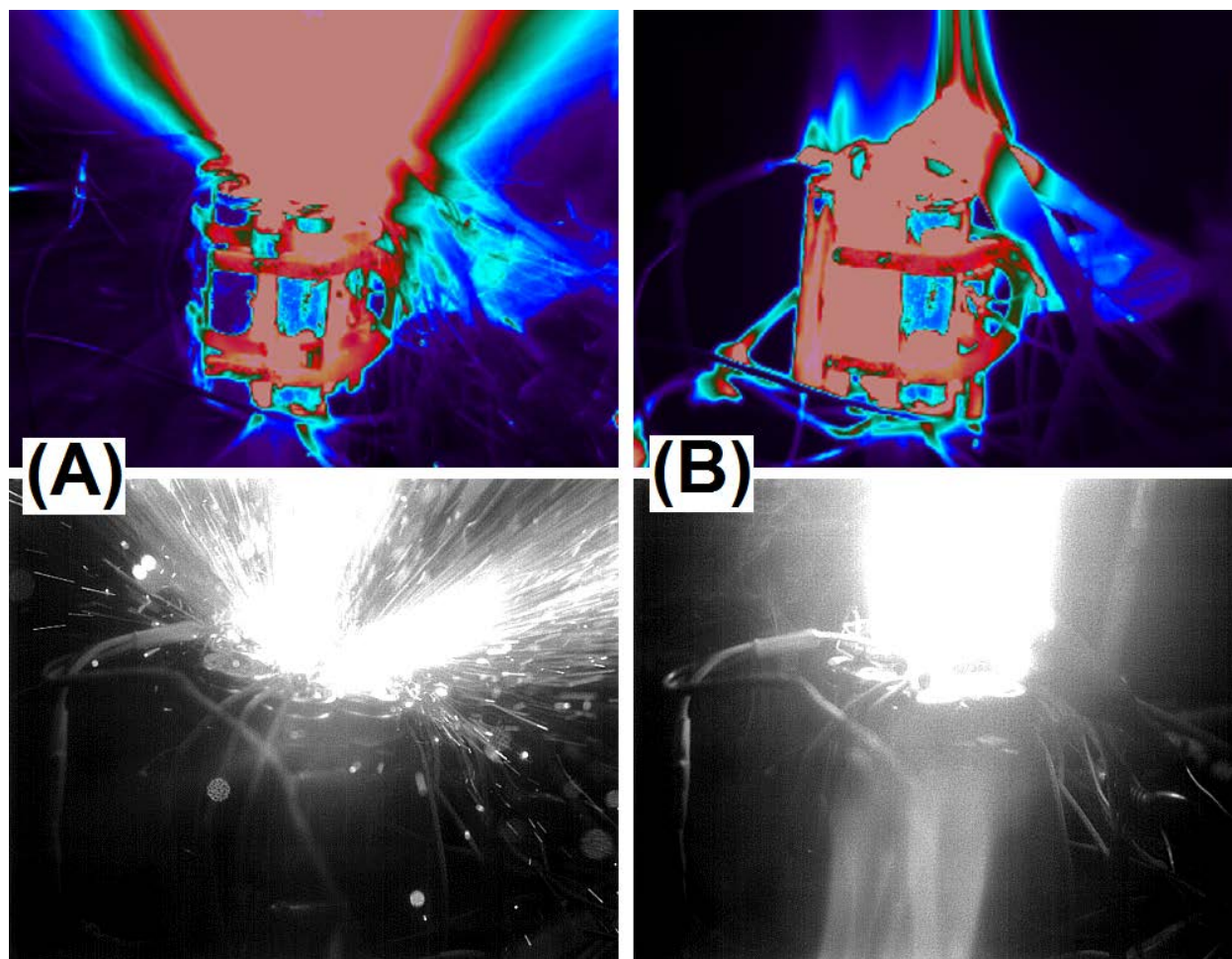


Figure 22: IR (top) and high speed (bottom) camera images of hex package 1 during failure event (A) at the beginning of the event during initial sparking/burst, and (B) after the initial failure incident where the package exhibited a slow-burning, sustained flame for several seconds. Active cell in the center was LiCoO_2 chemistry; abuse was 10A overcharge followed by heating from adjacent surrogate heater cell.

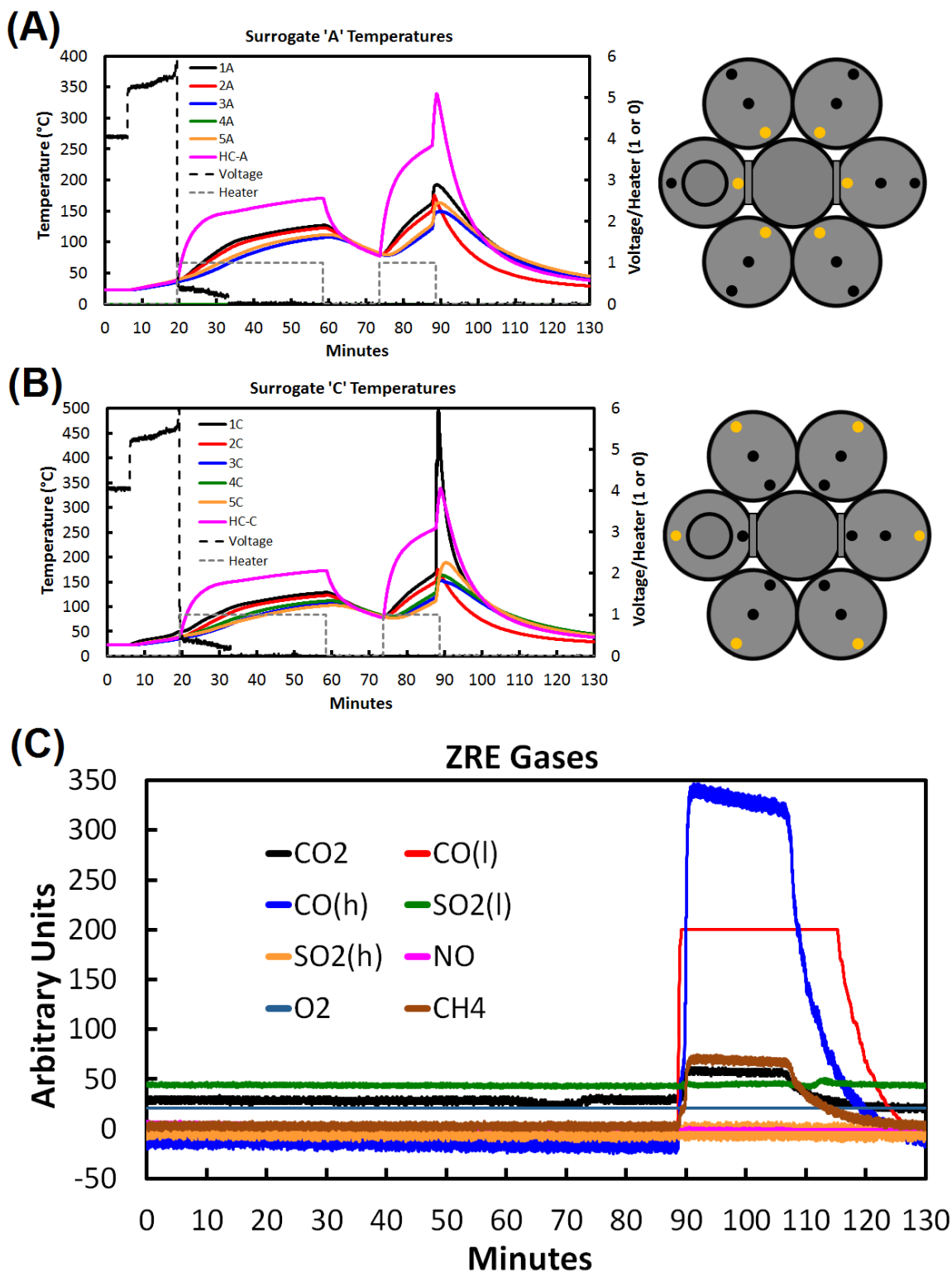


Figure 23: Hex package 1 thermocouple temperature readings for (A) 'A' position thermocouples and (B) 'C' position thermocouples, along with active cell battery voltage and heater on/off control versus time. Diagrams of hex package 1 with highlighted locations for corresponding temperature readings shown to the right of each plot (see Figure 14 for complete labels and numbering). (C) Detected gases from two ZRE real-time gas analyzers with respect to time. Test was 10A overcharge followed by heating from adjacent surrogate heater cell of LiCoO_2 active cell.

the 10A overcharge caused the voltage to drop once an internal safety mechanism had likely triggered, two stages of external heating were performed. The first was intended to result in thermal runaway and a failure event; however, it became evident that there was not enough heat being provided via the cartridge heater to initiate failure. The lack of a true failure event during this first unsuccessful heating stage was observed in the live camera video feeds, and also verified by the absence of any detected gases from the two ZREs shown in Figure 23C through the 80-minute mark. Therefore, the test was briefly suspended and the variable transformer controlling the cartridge heater was increased from its original setting of 30% to 40%. The test was then restarted with the higher heating rate and thermal runaway leading to failure was successfully initiated around the 90-minute mark.

Visually, the failure event for hex package 1 displayed some interesting behavior. First, a short (~1 second), violent, explosive venting of sparks occurred (Figure 22A), which was then followed by a longer (~30 seconds), slow-burning flame that originated from the active cell and spread to surrounding equipment (heat flux gauges, wires, etc.). Throughout the slow-burning flame, several pieces of hex package 1, including an entire surrogate cell, began to break off and fall away, ultimately resulting in a loss of the original hex package structure. This can likely be attributed to the construction of the hex package, which was held together with hot glue, since it was also observed leading up to the event that hot glue began to melt and drip downward from the package, thus leaving only the three-pronged clamp holding the package as the primary force keeping it together. For this reason, hex package 2 was later wrapped tightly in a hose clamp to ensure the structural integrity in the event of melting hot glue and battery failure/fire.

Surrogate cells were instrumented with three equally-spaced thermocouples to ideally try to observe temperature differences throughout the cell as heat propagated leading up to, during, and after a failure event. However, Figures 23A and B show starkly similar temperature-time curves for each individual surrogate cell in their respective 'A' and 'C' thermocouple positions. Neglecting locations where somewhat irregular and unpredictable temperature spikes appeared non-uniformly for all surrogates and thermocouples (around the failure event), with few exceptions the difference in temperatures between thermocouples 'A' and 'C' at all times was under 4%, and the majority of the time it was at or below 1%. This indicates a certain degree of redundancy in using three thermocouples per surrogate cell, and that perhaps it would be more instructive to look at heat propagation across multiple layers of surrogate cells rather than through a single cell itself. For future tests, this will become a primary focus, and multiple configurations of larger-scale cell packages will be explored.

While not much significant information was gathered from temperature distributions within individual surrogate cells, comparing temperatures of different surrogates to one another did warrant investigation and several observations can be made. First, an abnormally high spike in temperature seen in Figure 23B for thermocouple 1C at the point of failure may have arisen from a localized element catching fire or a heterogeneous burst of hot sparks/gases in that particular direction. Second, the rate of cooling for surrogate cell 2 appeared to be significantly quicker than all other surrogates. This is likely due to the aforementioned cell breaking off and falling away from the rest of hex package 1, meaning that the particular cell that fell away can be

specifically identified as surrogate cell 2. By releasing from the rest of the hot cell package, surrogate cell 2 was able to cool more rapidly from ambient air similarly to the behavior seen in the single cell test (Figure 19). Third, temperatures for HC-A (Figure 23A) and HC-C (Figure 23B) were around 60-80% higher on average than all other surrogate cell temperatures, which was expected since these two thermocouples were situated in the surrogate heater cell directly next to the cartridge heater. Finally, peak temperatures during the failure event in surrogate cells 1 and 5 were 14% higher on average than those in surrogate cells 3 and 4 (surrogate cell 2 excluded due to its breaking away from the hex package). Following the previous point, this also makes sense in light of the proximity of surrogate cells 1 and 5 to the surrogate heater cell (see Figure 14 for locations), whereas surrogate cells 3 and 4 were farther away and therefore received less direct exposure to heat being propagated through the hex package.

The second hex package test (denoted “hex package 2”) was performed in a similar manner to the hex package 1 test where the LiCoO₂ battery was overcharged with a 10A current followed by external heating from a cartridge heater in the adjacent surrogate heater cell. IR and high speed camera images of the ensuing failure event are shown in Figure 24, and temperature, heat flux, and gas detection data are shown in Figure 25. While the hot glue in hex package 2, much like hex package 1, melted and dripped out leading up to the failure event, the actual event observed for hex package 2 showed distinctive differences from hex package 1. Prior to the active cell bursting, wisps of vapor could be seen (Figure 24A) rising from the cells, and a relatively uniform and predictable manner of temperature increase was observed both in the IR camera images and the temperature-time curves. The observed vapor was likely the result of normal cell venting due to increased internal pressure from gas formation as the cell was heated. Once the failure event commenced, the cap of the active cell was expelled in the initial rupture, along with sparks, flames, and additional shrapnel that persisted for only a few seconds. Due to the hose clamp that was affixed around the hex package, no cells became detached during the test and the structural integrity of all cells, save the exploding active cell, was maintained.

Similarly to hex package 1, thermocouple temperatures for HC-A in the surrogate heater cell for hex package 2 were as much as 45-75% higher than the temperatures in the surrounding surrogate cells (Figure 25A, excluding the obvious and abnormally large spike in thermocouple 5A around the failure event at the 38-minute mark). Peak temperatures in surrogate cells 1 and

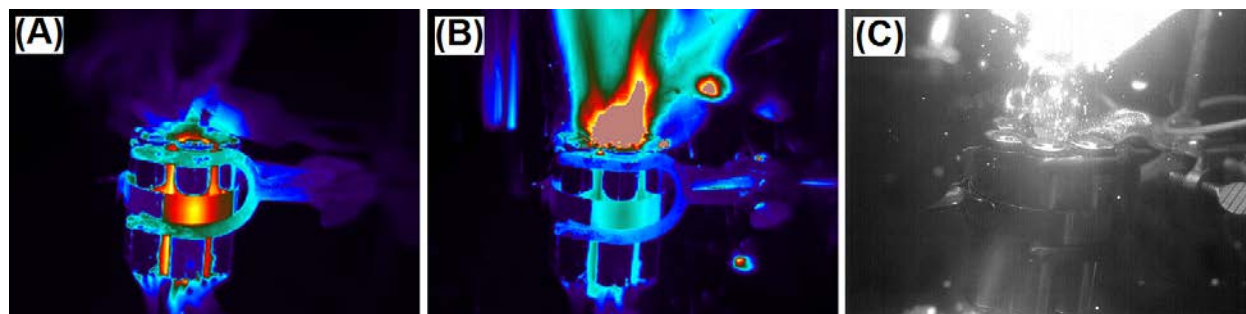


Figure 24: IR camera images (A) just before and (B) during failure event, and (C) high speed camera image during failure event of hex package 2. Active cell in the center was LiCoO₂ chemistry; abuse was 10A overcharge followed by heating from adjacent surrogate heater cell.

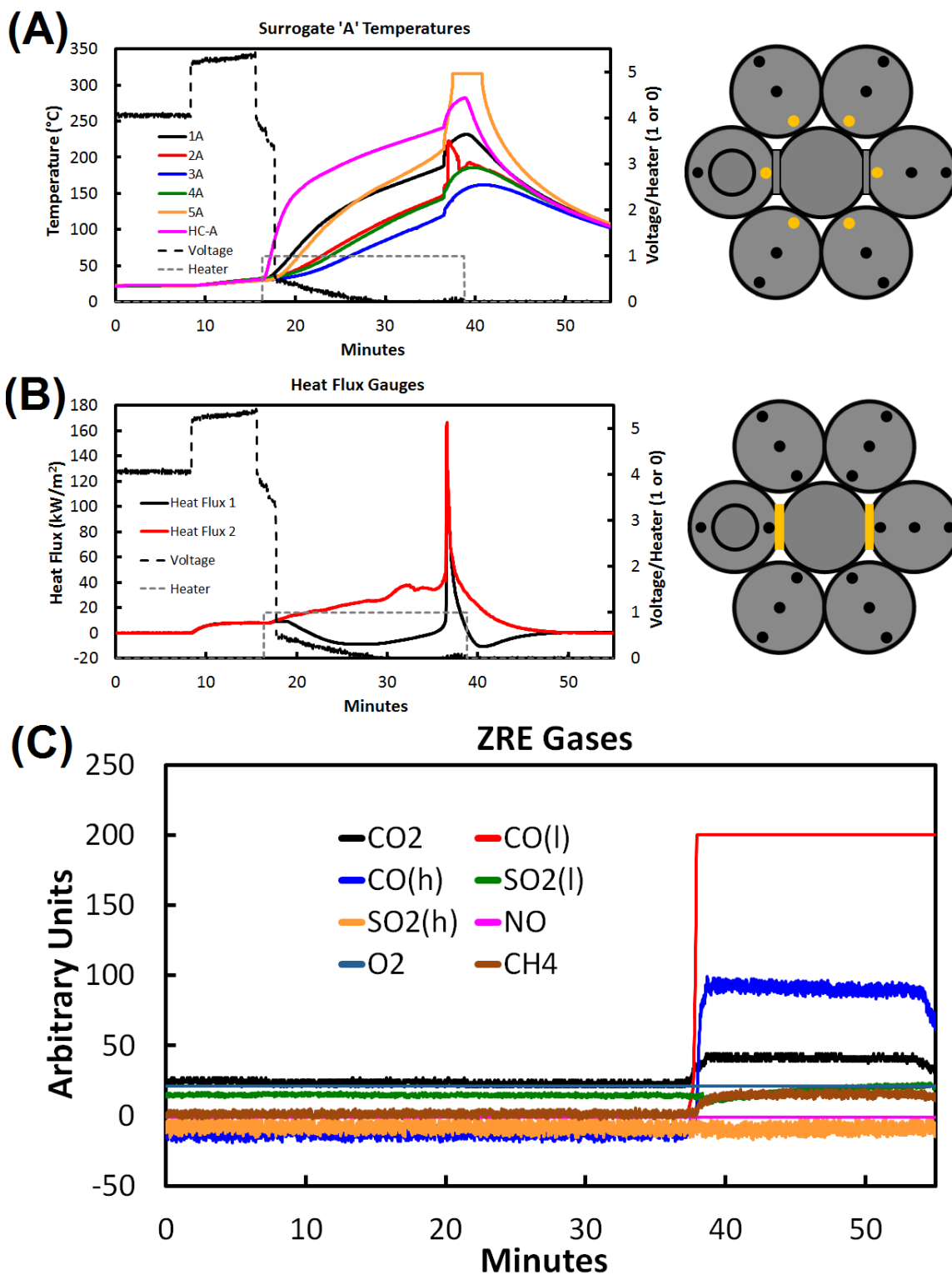


Figure 25: (A) Hex package 2 thermocouple temperature readings for 'A' position thermocouples, and (B) heat flux gauge measurements, along with active cell battery voltage and heater on/off control versus time. Diagrams of hex package 2 with highlighted locations for corresponding temperature readings shown to the right of each plot (see Figure 14 for complete labels and numbering). (C) Detected gases from two ZRE real-time gas analyzers with respect to time. Test was 10A overcharge followed by heating from adjacent surrogate heater cell of LiCoO₂ active cell.

5 were also as high as around 30% greater during the failure event than surrogate cells 2, 3, and 4, though peak the spike for 5A appeared to max out the readable temperature for the thermocouple and therefore its exact peak temperature was not attainable from the data. These temperature differences, again similarly to hex package 1, resulted from proximity to the cartridge heater in the surrogate heater cell (and in the case of HC-A, being inside the cell and directly adjacent to the cartridge heater).

Hex package 2 heat flux gauge data shown in Figure 25B revealed several stages leading up to, during, and after the failure event. Since the 'A' positions for both heat flux gauges were directly adjacent to the center active cell and heat flux is determined going from 'A' to 'B', positive heat flux values in Figure 25B signify a net flow of energy away from the active cell; conversely, negative heat flux values mean energy is flowing into the active cell at that heat flux location. Beginning around the 9-minute mark when the 10A overcharge was initiated until about the 17-minute mark when an internal safety device likely triggered followed by the heater being turned on, both gauges recorded slightly positive heat flux values of around 15 kW/m² indicating that the overcharging was producing heat inside the active cell that was propagating out to the surrounding surrogate cells. Once the heater was turned on at the 17-minute mark until around the 36-minute mark, the heat flux gauges diverged, with gauge 1 dipping to negative values and gauge 2 becoming increasingly more positive. This makes sense in light of the heat that was being produced from the cartridge heater and the physical configuration of hex package 2. Schematically, heat was propagating from left-to-right, meaning for heat flux gauge 1 energy flowed into the active cell producing negative values, and for heat flux gauge 2 energy flowed out of the active cell producing positive values. After the 36-minute mark, thermal runaway inside the active cell began to take place, and tremendous heat was generated leading up to, and including, failure. The heat expelled during this event far exceeded the heat being provided from the cartridge heater, thus causing a net flow of energy out of the active cell at all points and producing positive heat flux values for both gauges. Additionally, since there was still residual heat from the cartridge heater moving in the same direction at heat flux gauge 2 (out of the cell, or left-to-right), this explains why the additive peak heat flux reading (166 kW/m²) for heat flux gauge 2 was higher than for heat flux gauge 1 (112 kW/m²). Finally, after the failure event had exhausted all heat generation inside the active cell around the 40-minute mark, residual heat from the cartridge heater briefly caused a negative heat flux reading for gauge 1 and a positive value for gauge 2 once more until the system cooled off and equilibrated back to room temperature.

Detected gases from the two ZRE real-time gas analyzers shown in Figure 25C were virtually identical to those seen in hex package 1 (Figure 23C) and the single cell test (Figure 19B): CO, CO₂, and CH₄, with a trace signal from SO₂. As previously described, internal pressure and a limited quantity of O₂ likely led to mostly incomplete combustion producing CO, and decomposition of electrolyte likely led to the formation of CH₄ and possibly some CO as well. Also, again, the detection of SO₂ was interesting since there was no reported source of sulfur, and as before the SO₂ signal can likely be explained by cross sensitivity of the CH₄ sensor in the ZRE which can cause false SO₂ detection. FTIR results for hex package 2 are shown in Figure 26,

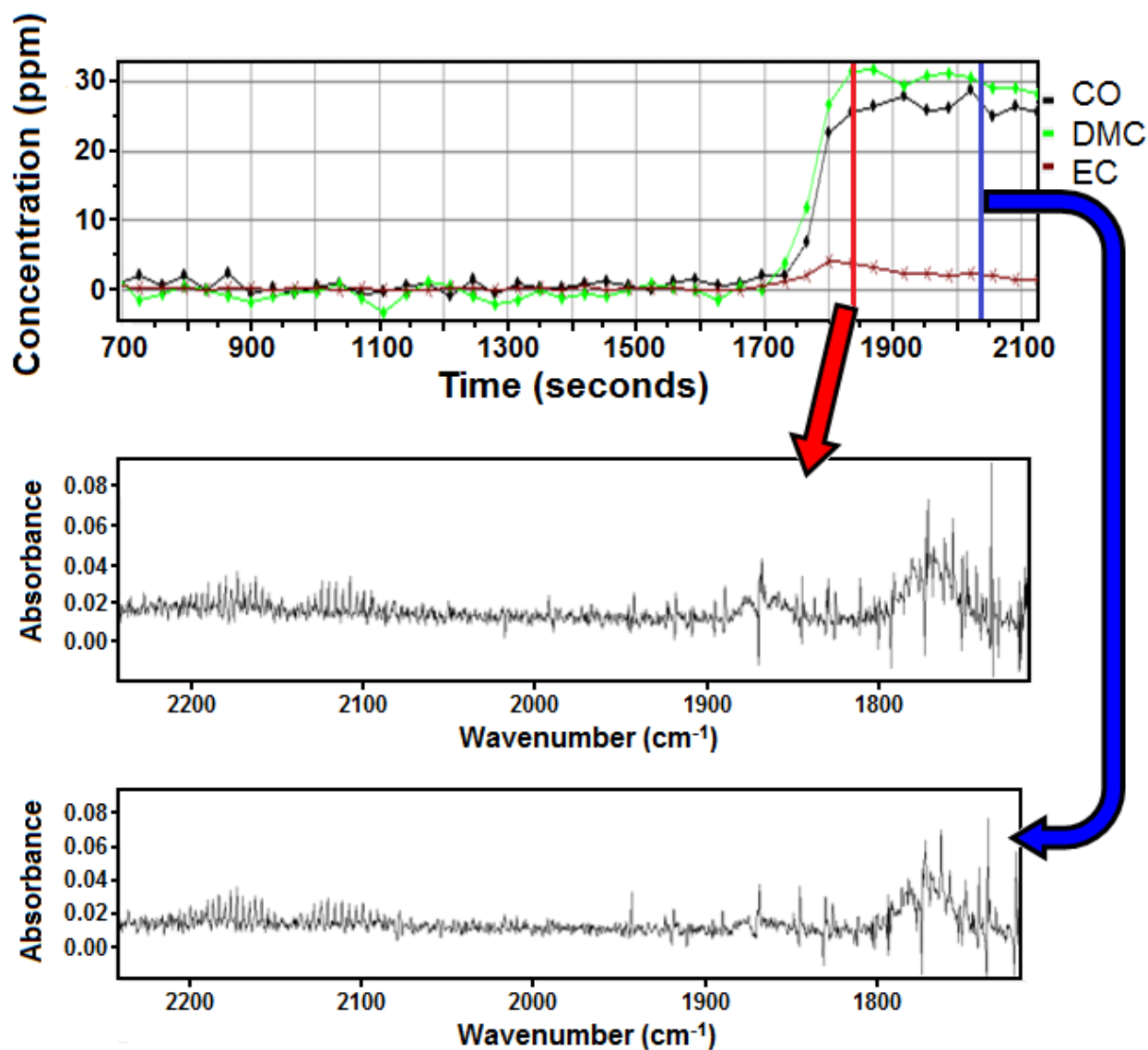


Figure 26: Fourier Transform Infrared Spectroscopy results from hex package 2 test. Species detected were carbon monoxide (CO), and electrolyte components dimethyl carbonate (DMC) and ethylene carbonate (EC). Top plot shows concentrations of these three species over the course of the test, and the bottom two plots show individual FTIR spectra at the beginning of the failure event and after a few minutes elapsed. Test was 10A overcharge followed by heating from adjacent surrogate heater cell of LiCoO_2 active cell.

and the first significant observation from FTIR was that presence of CO was confirmed. Additionally, around 5-30 ppm of electrolyte components dimethyl carbonate (DMC) and ethylene carbonate (EC) were detected during the failure event via FTIR, having been flashed and expelled due to extreme heat during the failure event without decomposition or combustion. About three minutes after the initial failure event, the concentration for EC began steadily decreasing, likely due to its high boiling point ($\sim 261^\circ\text{C}$) resulting in lower volatility and condensation as temperatures began to drop. The concentrations of CO and DMC, however, remained relatively stable in the few minutes following the failure event.

5.0 Conclusions

Cell-to-cell failure events and propagation in lithium-ion batteries have been studied, and several tests have been conducted and analyzed to determine mechanisms of failure, heat propagation, physical characteristics, and qualitative observations. These tests took advantage of a 5-m³ two-man decompression chamber at NRL-CBD that has been re-purposed with various pieces of equipment and instrumentation to enable safe monitoring and studying of lithium-ion battery failure events. A command station was set up to remotely control all chamber functions, thermocouples, and cameras through a Gigabit-enabled LAN with two CompactRIOs and several multi-port switches. Using two different 18650-type lithium-ion battery chemistries and several non-active surrogate cells fitted with thermocouples and/or cartridge heaters, both single cell and multi-cell packages were tested to see the response during a typical failure event, and analyzed to determine how heat was propagated to neighboring cells before, during, and after the event.

Two hex packages each containing one LiCoO₂ active cell were stressed to the point of failure and studied, and the observations from each failure event were very different. The first event occurred in essentially two stages: a quick, explosive burst of sparks and shrapnel, followed by a longer, slow-burning flame that spread to surrounding equipment. The second event, on the other hand, simply caused an explosive, sparking burst of the battery cap for only a few seconds, without any sustained fire afterwards. The heterogeneity in these two tests highlights a significant safety issue involved with lithium-ion batteries in large packs. There is not a great deal of predictability as to the precise manner in which a battery will fail when exposed to aggressive conditions, and this can be extremely hazardous as significant heat produced from, for example, a longer-burning fire may cause additional active cells to undergo failure and result in a catastrophic chain reaction.

One of the biggest challenges with these tests and inducing failure events was with the internal safety devices in the batteries, including PTCs and/or CIDs. Since these features are designed to prevent overcharge abuse, it was not possible to induce failure simply by applying a large voltage or current for an extended period of time as the safety device was triggered and the circuit was opened, allowing the battery to self-cool. For all failure inducements, a surrogate heater cell equipped with a cartridge heater that was controlled by a variable transformer was used to provide constant heat until a failure event was witnessed. This is a problem since many large-scale lithium-ion battery packs for military applications may not have these individual safety devices, and as such may be brought to thermal runaway and eventually failure simply by an overcharge abuse. Therefore, it will become crucial in future tests to try and isolate overcharging and overheating as separate mechanisms for causing battery failure to more accurately simulate real-world conditions.

Another future consideration that will need to be addressed is a measure of the internal condition of the battery during a test, specifically its temperature and state of health/state of charge. While it is useful to have heat flux gauges and thermocouples affixed on and near the active cell, these can only give measures of temperature and energy flow at the surface of the

cell at best. Often during a battery failure event, the internal temperature can be larger than the surface temperature by as much as 50-100°C, particularly as thermal runaway begins to accelerate. For this reason, to be able to accurately predict when an active cell will fail will require a more in-depth analysis of the internal condition rather than simply measurements at the surface of the cell casing. These issues will be addressed and results will be forthcoming.

6.0 References

- [1] Tippmann, S.; Walper, D.; Balboa, L.; Spier, B.; Bessler, W. G. "Low-temperature charging of lithium-ion cells part 1: Electrochemical modeling and experimental investigation of degradation behavior." *J. Power Sources* **252** (2014) 305-316.
- [2] Keyser, M.; Smith, K.; Pesaran, A.; Ireland, J.; Kim, G.; Long, K.; Neubauer, J. "Battery Thermal Modeling and Testing." *U.S. DOE Hydrogen Program and Vehicle Technologies Program Annual Merit Review & Peer Evaluation Meeting*, 9-13 May 2011, Arlington, Virginia.
- [3] Wu, B.; Yufit, V.; Marinescu, M.; Offer, G. J.; Martinez-Botas, R. F.; Brandon, N. P. "Coupled thermal-electrochemical modelling of uneven heat generation in lithium-ion battery packs." *J. Power Sources* **243** (2013) 544-554.
- [4] Ahmad, A.; Pesaran, Kim G.-H.; Smith, K.; Santhanagopalan, S.; Lee, K.-J. "Overview of Computer-Aided Engineering of Batteries and Introduction to Multi-Scale, Multi-Dimensional Modeling of Li-Ion Batteries." *U.S. DOE Hydrogen Program and Vehicle Technologies Program Annual Merit Review & Peer Evaluation Meeting*, 14-18 May 2012, Arlington, Virginia.
- [5] Haupt, T. A.; Henley, G.; Parihar, B. S.; Kirkland, R.; Floyd, J.; Scheffey, J.; Tatem, P. A.; Williams, F. W. "User Manual for Graphical User Interface Version 2.10 with Fire and Smoke Simulation Model (FSSIM) Version 1.2" *NRL Memorandum Report NRL/MR/6180-10-9244* of 10 May 2010.
- [6] Floyd, J. E.; Hunt, S. P.; Williams, F. W. "Fire and Smoke Simulator Version 1.7 (FSSIM) *NRL Ltr Rpt* 6104/0003 of 02 April 2012.
- [7] ASAP: Advanced Survivability Assessment Program Naval Surface Warfare Center, Carderock Division, Bethesda, MD.
- [8] Lin, X.; Perez, H. E.; Mohan, S.; Siegel, J. B.; Stefanopoulou, A. G.; Deng, Y.; Castanier, M. P. "A lumped-parameter electro-thermal model for cylindrical batteries." *J. Power Sources* **257** (2014) 1-11.
- [9] Forgez, C.; Do, D. V.; Friedrich, G.; Morcrette, M.; Delacourt, C. "Thermal modeling of a cylindrical LiFePO₄/graphite lithium-ion battery." *J. Power Sources* **195** (2010) 2961-2968.
- [10] Bandhauer, T. B.; Garimella, S.; Fuller, T. F. "A critical review of thermal issues in lithium-ion batteries." *J. Electrochem. Soc.* **158** (2011) R1-R25.
- [11] Belov, D.; Yang, M.-H. "Investigation of the kinetic mechanism in overcharge process for Li-ion battery." *Solid State Ionics* **179** (2008) 1816-1821.
- [12] Williams, F. W.; Pham, H. V.; Durkin, A. F.; Gould, B. D. "The Heat Released Rate from Lithium Polymer and Lithium-Iron Phosphate Batteries Thermally Stressed" *NRL Ltr Rpt* 6104/0006 of 28 April 2010.

- [13] Back, G. G.; Williamson, J.; Williams, F. W. "Lithium Battery Casualty Mitigation System (LBCMS) Development – Potential Gas Production Caused by Electrolysis" *NRL Ltr Rpt* 6104/0015 of 09 July 2010.
- [14] Williams, F. W.; Durkin, A. F.; Winchester, C. S.; Pham, H. V. "Tests to Support Development of a Lithium Battery Casualty Mitigation System (LBCMS) - Phase 1: Heat Release Rate Baseline Data" *NRL Ltr Rpt* 6104/0017 of 13 September 2010.
- [15] Back, G. G.; Durkin, A. F.; Nguyen, X.; Pham, H. V.; Duncan, S.; Winchester, C. S.; Gratz, J.; Williams, F. W. "Lithium Battery Casualty Mitigation System (LBCMS) Development Tests – Brass Board Tests (Quick Look)" *NRL Ltr Rpt* 6104/0009 of 05 July 2011.
- [16] Williams, F. W.; Pham, H. V.; Durkin, A. F.; Winchester, C. S.; Back, G. G. "Lithium Battery Casualty Mitigation System (LBCMS) – Brass Board Test Results" *NRL Ltr Rpt* 6104/0015 of 14 November 2011.
- [17] Williams, F. W.; Rose-Pehrsson, S. L. "A Test Plan for the Tips Program to Measure the Gaseous Species Production of Generic Lithium Batteries Exposed to Thermal Abuse" *NRL Ltr Rpt* 6104/0005 of 19 April 2010.
- [18] Balakrishnan, P. G.; Ramesh, R.; Prem Kumar, T. "Safety mechanisms in lithium-ion batteries." *J. Power Sources* **155** (2006) 401-414.
- [19] NASA Engineering and Safety Center (NESC) Technical Report RP-08-75, Version 1.0, Part I – Volume II, NESC Request No.: 06-069-I, 10 July 2008.
- [20] Love, C. T.; Swider-Lyons, K. "Impedance diagnostic for overcharged lithium-ion batteries." *Electrochem. Solid-State Lett.* **15** (2012) A53-A56.
- [21] Padhi, A. K.; Nanjundaswamy, K. S.; Goodenough, J. B. "Phospho-olivines as positive-electrode materials for rechargeable lithium batteries." *J. Electrochem. Soc.* **144** (1997) 1188-1194.